PROBING THE INITIAL STAGES OF SOLID STATE REACTIONS

Sonia Pin

Alma Ticinensis Universitas – Università degli Studi di Pavia

Université Joseph Fourier de Grenoble

Studio dei primi istanti delle reazioni solido - solido

Probing the initial stages of solid state reactions

Etude des instants initiaux des réactions solide – solide

Sonia PIN

DOTTORATO DI RICERCA in Scienze Chimiche
XXII CICLO
Settore scientifico disciplinare: CHIM02

ECOLE DOCTORALE Matériaux et génie des procédés
ECOLE DOCTORALE N°228

Relatore (Italy): Prof. Paolo GHIGNA – Università degli Studi di Pavia
Directeur de thèse (France) : Prof. Michel DUCLOT – Université Joseph Fourier

Questo messaggio lo dedichiamo ai folli. A tutti coloro che vedono le cose in modo diverso. Potete citarli. Essere in disaccordo con loro. Potete glorificarli o denigrarli, ma l'unica cosa che non potete fare è ignorarli. Perchè riescono a cambiare le cose. E mentre qualcuno potrebbe definirli folli, bisogna vederne il genio. Perchè solo coloro che sono abbastanza folli da pensare di poter cambiare il mondo, lo cambiano davvero".

Mahatma Gandhi

... A Me... A Te... A Noi...

Riassunto

Il presente lavoro di tesi di dottorato intitolato “Studio dei primi istanti delle reazioni solido – solido” è stato realizzato nel quadro di una tesi in co-tutela franco-italiana sotto la doppia direzione dell’Alma Ticinensis Universitas – Università degli Studi di Pavia e dell’Università Joseph Fourier di Grenoble. Si è svolto principalmente al Dipartimento di chimica – fisica “M. Rolla” dell’Università di Pavia, sotto la supervisione del Prof. Paolo GHIGNA. La parte francese si è svolta sotto la supervisione del prof. Michel DUCLOT al *Laboratoire de Electrochimie et de Physico-Chimie des Matériaux et des Interfaces – LEPMI* (UMR 5631, CNRS, Grenoble-INP, UJF). Inoltre, i lavori sperimentali di studio della cinetica delle reazioni tra ossidi sono stati svolti presso lo *European Synchrotron Radiation Facility* (E.S.R.F., Grenoble, France), sotto la supervisione del Dr. Francesco D’ACAPITO.

La tesi è organizzata in sette capitoli. L’introduzione fornisce una visione generale sulle conoscenze delle reazioni allo stato solido, sia dal punto di vista termodinamico che da quello del trasporto della materia. Il primo capitolo fornisce il punto della conoscenza sulle reazioni solido-solido e mostra l’interesse per la conoscenza degli istanti iniziali. Proprio questo punto costituisce l’originalità del lavoro sviluppato. Nel capitolo 2 sono presentate le strategie di analisi dei dati e il tipo di modello sperimentale (film sottile di ossido depositato su un substrato monocristallino).

Il capitolo 3 è dedicato alla crescita epitassiale del film sottile di ossido tipo MO, (M = Ni, Zn, Mn), depositato mediante RF-magnetron sputtering. Il campione così preparato è poi cotto in modo da avere una buona orientazione del film.

La tecnica di X-ray Absorption Spectroscopy (XAS) e Fluorescence X-ray Absorption Spectroscopy (Fluo-XAS) sono presentati nel capitolo 4 come la beamline GILDA BM08 di ESRF, dove sono stati svolti gli esperimenti che hanno permesso l'identificazione di almeno un nuovo composto cristallino. Sulla beamline ID24 (ESRF) sono state realizzate le misure di micro X-ray Absorption Near Edge Spectroscopy (micro-XANES) (capitolo 5). Sulla beamline ID03 (ESRF) sono invece state svolte le misure di diffrazione superficiale (capitolo 6).

Un passo avanti nell'analisi della superficie viene effettuato nel capitolo 7 dove le misure di Atomic Force Microscopy (AFM) e di Diffrazione Elettronica (ED) mostrano impressionanti cambiamenti della morfologia superficiale dei film di ossido (capitolo 8).

Questo lavoro ha permesso un approccio innovativo per la comprensione dei meccanismi delle reazioni interfacciali a livello atomico. Questi risultati possono essere un contributo importante per l'elaborazione di nuovi ossidi a livello nanometrico. Questa prospettiva lascia pensare all'apertura di una nuova via per lo studio dei meccanismi di reazioni allo stato solido in modo analogo alla femtochimica in fase gassosa.

Abstract

The work presented in this PhD thesis and entitled “Probing the initial stages of solid state reactions” has been mainly carried out under a *Convention de Co-tutelle de thèse* between France and Italy and the two universities, Alma Ticinensis Universitas – Università degli Studi di Pavia and Université Joseph Fourier de Grenoble. The work has been mainly carried out at the Department of Phisical – Chemistry “M. Rolla” of the University of Pavia under the supervision of prof. Paolo GHIGNA and the *Laboratoire de Electrochimie et de Physico-Chimie des Materiaux et des Interfaces* – LEPMI (UMR 5631, CNRS, Grenoble-INP UJF) under the direction of Prof. Michel DUCLOT. The work of study of the kinetic of the reaction between oxides was performed at the European Synchrotron Radiation Facility (E.S.R.F., Grenoble, France), under the supervision of Dr. Francesco D’ACAPITO.

The thesis is organized in seven chapters. The introduction presents the general concept of solid state reactions, under the point of view of the thermodynamic and of the matter transport. The first chapter shows what we know about reactions in the solid state and the high need for the understanding of the early stages nowadays. It’s this crucial point the one that shows the peculiarity of this work. In chapter 2 the analysis strategy and the model that have been choose (thin film onto a monocrystal) are presented along with the main options exploited during the PhD.

Chapter 3 is dedicated at the epitaxial growth of the thin film of oxide MO, (M = Mn, Ni, Zn), deposited by means of RF-magnetron sputter and subsequently the anneal and the reactions are carried out to have a good film orientation.

The X-ray Absorption Spectroscopy (XAS) technique and the Fluorescence X-ray Absorption Spectroscopy (Fluo-XAS) with the GILDA BM08 beamline (ESRF) are presented in chapter 4, whit the identification of at least a new crystalline compound. The ID24 beamline (ESRF) has been used for the micro X-ray Absorption Near Edge Spectroscopy (micro-XANES) experiment (chapter 5). The ID03 beamline (ESRF) has been used for the surface diffraction measurements (chapter 6).

A step forward in the surface analysis is presented in chapter 7 where the Atomic Force Microscopy (AFM) and Electron Diffraction (ED) techniques reveal an impressive change in the surface morphology of the reacted films (chapter 8).

This work has involved a completely new approach for the comprehension of the mechanisms in the interfacial reactions at atomistic level. These results may be an important contribution for the design of new oxides at nanometric scale. This perspective open a new way for the study of the mechanisms in solid state reactions similarly to femtochemistry in gas phase.

Résumé

Le présent travail intitulé « Etude des instants initiaux des réactions solide – solide » a été réalisé dans le cadre d'une thèse en co-tutelle franco-italienne sous le double sceau de Alma Ticinensis Universitas de Pavie et de l'Université Joseph Fourier de Grenoble. Il s'est déroulé pour l'essentiel au 'Département de Chimie-physique Mario Rolla' de l'université de Pavie, sous la direction du Prof. Paolo GHIGNA. La partie française c'est déroulé sous la direction du Prof. Michel DUCLOT au Laboratoire d'Electrochimie et de Physico-Chimie des Materiaux et des Interfaces - LEPMI (UMR 5631, CNRS, Grenoble-INP, UJF). De plus, les travaux expérimentaux du suivi de la cinétique des réactions oxyde - oxyde ont été réalisés au 'European Synchrotron Radiation Facility', (E.S.R.F, Grenoble, France), sous la direction du Dr. Francesco D'ACAPITO.

Le mémoire est subdivisée en 7 chapîtres. L' introduction fait un point général sur les connaissances des réactions entre solides tant du point de vue thermodynamique que du point de vue transport de la matière. Le première chapitre fait le point des connaissances de la cinétique des réactions solide – solide et montre l'intérêt de la connaissance des phénomènes aux instants initiaux. Ce point constitue la partie originale qui sera développé dans ce travail. Dans le chapître 2 sont présentés la stratégie d'analyse (rayonnement synchrotron, ajustement des données) ainsi que le système expérimental (film mince du matériaux étudie sur substrat monocristallin).

Le chapître 3 est consacrée a l'étude de la croissance épitaxiale des films minces d'oxyde de type MO, (M = Mn, Zn, Ni), à l'aide d'un système de déposition par

magnetron sputtering Radio Frequence (RF-magnetron sputter). L' échantillon obtenu est ensuite recuit pour l'homogéneité de l'orientation épitaxiale.

Les techniques X-ray Absorption Spectroscopy (XAS) et Fluorescence X-Ray Absorption Spectroscopy (fluo-XAS) sont présentées dans le chapître 4 ainsi que le faisceau synchrotron GILDA BM08 de l'ESRF, où ont été réalisées les expériences ce qui a permis l'identification d'au moins un nouveau composé cristallin. Sur le faisceau ID24 (ESRF) ont été réalisées les mesures de X-ray Absorption Near Edge Spectroscopy (micro-XANES) (chapître 5). Le faisceau ID03 (ESRF) a servi pour les mesures de diffraction superficielle (chapître 6).

Un pas en avant dans l'analyse de la surface est présenté dans le chapître 7 où les mesures par Atomic Force Microscopy (AFM) et par Electron Diffraction (ED) montrent des changements impressionnants de la structure et de la morphologie superficielle des films d'oxyde (chapître 8).

Ce travail a permis un approche performante pour la compréhnsion des mécanismes des réactions interfaciales au niveau de l'atome. Ces résultats peuvent être une contribution important pour l'élaboration de nouveaux oxydes à l'état nanometric. Cette perspective laisse penser à l'ouverture d'une nouvelle voie pour l'étude de mécanismes de réaction à l'état solide de façon analogue au réactions de femtochimie en phase gazeuse.

INDICE

INDEX

Sommaire

INTRODUCTION

"The scientist only imposes two things, namely truth and sincerity, imposes them upon himself and upon other scientists"

(E. Shrodinger)

The assessed theory of the kinetics of solid state reactions essentially describes the growth of a product phase enclosed between two grains of the reagent phases. In this treatment, various kinetic processes are considered, depending on the nature of reagents and product, the process variables, and the extent of the reaction [1]. In particular, as the reaction proceeds and the product layer becomes thicker, local chemical equilibrium is possibly attained at each interface so that the growth becomes kinetically controlled by diffusion in the product layer. Then, the theory predicts a parabolic growth law [2] (squared thickness proportional to time) and relates the experimentally accessible rate constant (the proportionality factor) to quantities that can be independently determined. Different mechanisms can be assumed depending on the structure elements or defects that are actually diffusing in the product phase, and the theory allows identification of the mechanism by comparing the rate constant to the diffusion coefficients of the mobile species or conversely to predict a reaction rate from the thermodynamic and transport properties of the product phase.

Useful additions to this general treatment take into account kinetic control by other processes, such as heat transport or interface mobility. The latter case is

particularly interesting as it extends the theoretical approach towards the initial stages of the reaction, when the product layer is thinner and the growth rate is constant (linear growth).

In both cases, *i.e.* diffusion control or interface mobility control, a basic assumption is that a product layer already exists. As matter of fact, practically nothing is presently known about the very early stages of the process, when the product layer is not yet formed and the chemical reactivity is entirely controlled by interfacial aspects. This quite surprising lack of basic understanding is related to the fact that the subject is largely unexplored mainly because of the lack of an established probe.

Solid state reactivity in its various aspects plays indeed a significant role in many different areas of science, such as Crystallography, Mineral Physics and Earth Sciences, Physical Metallurgy, Ceramic Science, Semiconductor Physics, Solid State Chemistry, but the basic knowledge and the main results (not to speak of the language itself) are not always well shared among the disciplines. Surface Science and Catalysis provide an ample background of knowledge on the transformations and reactions occurring at a free interface, while the processes occurring at the boundary between two condensed phases are an important topic in many of the scientific areas above quoted, for instance in the investigation of phase transformations or growth of thin films. All this knowledge provides important starting points but does not directly face the processes occurring when a *single* interface between two grains of the reagent phases is progressively turned into *two* different interfaces between each reagent and the newly formed product. So, for an extremely ample set of heterogeneous reactions, *i.e.* the

reactions involving two condensed phases as reagents and producing a different crystalline phase, the present state of art is that thermodynamics gives tools to predict whether or not the formation of a particular product can occur, and the assessed kinetic theory gives tools to predict the growth rate of this product when diffusion is the rate determining step. However, we do not really understand the mechanism through which this product is formed. This means that we have no general knowledge of the very basic aspects of the chemical reactivity in the solid state; for instance we ignore how and why a reaction actually goes towards one or another polymorph, a compound or a broad range solid solution, a stable or metastable product.

Quite impressively, the scientific community still needs an assessed agreement concerning the procedures and the aforementioned experimental probes required to investigate this topic, as well as a sound common background connecting the different areas that can seemingly provide important contributions to the advancement of knowledge, and that conversely can profit from that advancement.

Aim of the thesis is therefore to reach a basic understanding of the very initial stages of solid state reactions by organizing into a work team scientists with different backgrounds, in particular by adding to the core expertise in crystallography the required knowledge concerning solid state reactivity and defect chemistry, as well as the most effective characterization techniques, including those based on synchrotron radiation. We want to make clear that the main objective is to contribute to the advancement of knowledge in a very basic but somehow unexplored area of science which is at the crossroad of many disciplines. The objective can profit from many

sparse insights on the role of interfacial reactive steps so far available in the scientific literature on topics that are differently related to the subject of the present work, and is eventually achieved by combining into an original methodology the theoretical approaches and experimental tools coming from those different scientific areas.

The thesis is expected to have a strong impact on Mineral Physics and Earth Sciences. Geological history has been deciphered so far mainly by looking for markers of P-T-t paths in rocks, i.e. physicochemical responses of the minerals to, and fingerprints in minerals of, P-T-t changes. Microstructures and microtextures, which concern the small-scale arrangements of mineral species in rocks, are interesting in this respect because can be used in tracking back the conditions of such changes in view of the transformation mechanisms they suggest. It is their non-equilibrium nature that makes them particularly useful in tracking mineral behaviour.

Topological studies of microstructures and nanostructures (nature, size, mutual orientation of crystals, shape and orientation of their interface, etc.) of *frozen-in mineral reactions* provide significant evidence and are carried out to determine the types of reactions taking place in rocks. However, the interpretation of experimental data is subject to uncertainties. The recognition of the clues and evidences is tributary to the strength of the link that exists between the object and the mechanism. The present thesis is expected indeed to strengthen such link by giving new and fundamental insight into the mechanisms of solid state reactions.

The thesis is also expected to have a strong impact on the methods of preparing new crystalline materials or, more generally, on solid state synthesis. Generally speaking, this seems quite obvious, but actually requires a few comments as many areas of the current research on new materials do not clearly show such a strong demand for a better understanding of the very basic aspects of solid state reactivity. In this area, the synthetic activity actually receives far less attention than property characterization, and is frequently done on a very empirical basis; a rational approach, when present, is mostly oriented to understanding the thermodynamic aspects or optimizing a reaction rate. The nature of the reaction product appears quite obvious in almost all cases, so that there is seemingly no interest in understanding how and why a given product nucleates. When the products have more complex crystal structures and composition, the chemical reaction requires a significant reorganization of the structure elements, and the situation changes. Although not strictly pertinent to the topic under discussion, a very impressive example of the role of structural complexity in controlling the nature of a product is the production of a metallic glass from fast cooling of a melt. This process is essentially based on hindering crystallization of thermodynamically more stable compound phases, which is found to become progressively more difficult as more components and complex intermetallic structures are involved.

To sum up, the interest for a better understanding of the very early stages of solid state reactions is a current issue in the mineralogical community and is expected to propagate rapidly to materials science and solid state synthesis, where the interest is seemingly confined at present to specialized areas. Concerning the high temperature oxide superconductors, for instance, an ample variety of increasingly complex structures are under investigation, and current research already faces the difficulty of planning an

effective synthetic protocol using conventional solid state synthesis (sometimes known as “ceramic” synthesis). The same situation is expected in the near future in many other areas of materials science and solid state synthesis, as more complex crystalline phases with many different structural sites and complex stoichiometries (even neglecting doping) are progressively receiving attention (multiferroic materials and materials for spintronics being among the most pertinent examples) because of the very sophisticated functional properties so achieved or the possibility of combining in a single phase functional properties peculiar of significantly different compounds.

We finally note that understanding how the interfaces between condensed phases and their time evolution affect chemical reactivity is nanoscience by itself, so that it is almost impossible to quote all the expected connections of this research thesis with nanosciences and nanotechnology. In particular, a better understanding of these aspects is expected to provide strong impact on the knowledge of the chemical mechanisms underlying the deposition of thin films on various substrates, a preparative technique that spans a broad range of applications such as catalysis, photoluminescence, spintronics, information storage (magneto-resistance and related properties).

To introduce the central topic of the thesis, we note that the crucial role played by the interfacial free energy in heterogeneous reactions has been evidenced mainly by means of local inspections (for example, by means of TEM) of interfaces between bulky materials. It is well established that nucleation and growth of the product phase from a couple of reactants in the solid state is constrained by more factors than ‘free’ nucleation and growth from fluid media. The structural relationship between the two

phases controls the interfaces which in turn control the growth of the new phase and its spatial and orientational relationships with the parent phases.

In the case of a tight seed/host crystal boundary, the lowest activation energies of nucleation are realized (i) for a specific orientation of the seed to the host (topotaxy) and (ii) in the case of minimum stress/strain along and across the interface boundaries. A good coincidence of translational lattices and similarities in their atomic structures are in fact expected to favour nucleation since the reactant/product interface energy is lowered.

Because of the critical role of interface, it is possible to conceive to maximise and tune its effect. First, the role of the interface can be maximised by using one of the reactant in form of films of different thicknesses. Second, three different regimens can be explored and clarified:

1. For the very thin films, the reactive system is quasi-2D: the interfacial term dominates the overall free energy. Different products can be thermodynamically stabilised by the interfacial free energy: for given structures and compositions the effect is controlled by the topotactical relationships and is different for different interfaces (Fig. 1a). This has been recently evidenced by a preliminary study by the proposing team.

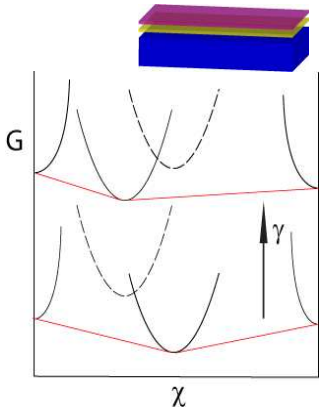

FIG. 1 Effect of the interfacial free energy (γ) on the relative stability of stable and metastable compounds (referred to the bulk, lower part of the diagram). The dashed lines refer to the less stable phase both in the bulk and in presence of interfacial free energy. The reactive system in this regime is also depicted.

2. For intermediate thickness, once the final phase has nucleated, interfacial movement is the rate determining step: topotaxy and interfacial free energy control the rate of the reaction.

3. For thick reaction layers, diffusion is the rate determining step and the interfacial term is negligible (Fig. 1b).

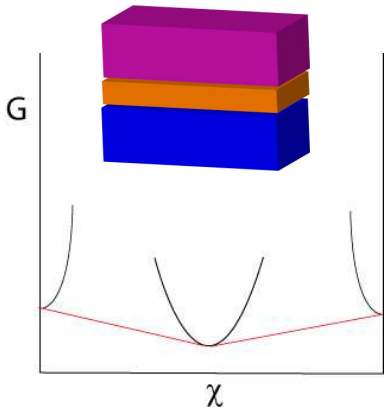

FIG. 2 In the diffusion controlled regime, the reactive system is shown with reactants and product layer in between.

In other terms, with respect to the bulk contribution, the interfacial contribution to the free energy of a layer decreases as the thickness increases. We can switch from a situation where the interfacial contribution is the largest to another where bulk contribution rules the process, that is from a quasi–2D to a 3D reactive system. We expect that the transitions between the regimes could be directed towards different products and investigated by changing the dimensionality of the reactive couple. To the best of our knowledge, this approach towards the reactivity in the solid state is completely original.

REFERENCES

[1] M. Cournil and G. Thomas (1982) *J. Chim. Phys.* **79**, 729.

[2] M. Cournil and G. Thomas (1977) *J. Chim. Phys.* **74**, 545.

1. SOLID STATE REACTIONS: THE NEED TO KNOW "THE BEGIN"

"There are two ways to live your life.
One is as though that nothing is a miracle.
The other is as though everything is a miracle."

(A. Einstein)

1.1 - SOLID STATE REACTIONS: INTRODUCTION

The concept of *Solid State Reactions* interests and inspires scientists worldwide. Solid State Reactions (SSR) [1-3] are of extreme interest both for technological applications and from the point of view of basic science. On one side, many important materials are currently prepared by solid state synthesis [4], for example almost all ceramic materials; on the other side, reactions in the solid state occur in many geological processes such as mineral metamorphism.

Nowadays the idea of reactions in the solid state is widespread in chemistry and related disciplines. We can refer to solid state reactions with "modern" words and concepts. A solid state chemical reaction in the classical sense occurs when local transport of matter is observed in crystalline phases. This definition does not means that gaseous or liquid phases may not take part in solid state reactions. However, it does means the reaction product occurs in a solid phase [5].

If the reactants are brought together at a constant pressure and temperature in a closed system, than the reaction will takes place spontaneously if the Gibbs free energy

of the system is decreased. During the course of a solid state reaction, there are local changes of the chemical potentials of the individual components *i* of the crystal. In the narrow sense, solid state reactions are characterized by the diffusion of atoms of type *i* (or of ions of type *i*) with charge z_i in chemical or electrochemical potential gradient.

Thus, the local changes of partial molar free energies of the various type of particles are the driving forces for chemical reactions in the solid state and the rate of diffusion is proportional to the driving force by means of a factors of proportionality called transport coefficient.

The transport of matter in the solid state, and thus also the reactivity of solids, are dependent upon the mobility of the individual particles in the structure. Every case of mass transport in solid phases is directly dependent upon deviation from ideal crystalline order. The rate constants in crystalline phases are directly related to the atomic disorder and the higher atomic disorder, the higher is the corresponding transport coefficient.

Solid state reactions are divided into the following groups:

1. homogeneous reactions
2. reactions in single phase inhomogeneous systems
3. heterogeneous reactions

Chemical reactions between solid crystalline materials are in general exothermic because of the high degree of order of crystalline phases, which means that the entropy difference between these phases is relatively small.

If two substances react with one another to form one or more product phases which are separated from the reactants and from other by phase boundaries, then a heterogeneous solid state reaction is said occur [6]. The simplest product phases are binary, as in the reaction equation

$$nA + mB \rightarrow A_nB_m$$

The reaction product separate the reactants from one another, and the reaction proceeds by diffusion of the participating components through the reaction product. For very low solubility of the reactants in the reaction product the particle fluxes are locally constant, and as long as local thermodynamic equilibrium is maintained at the phase boundaries, a parabolic growth law results.

From a single crystal of AO and a single crystal of B_2O_3, a partially monocrystalline spinel AB_2O_4 is formed and in this case the fluxes of the components in the reaction product, responsible for the advancement of the reaction, are fluxes of charged particles. Therefore, in order to preserve local electrical neutrality, the fluxes of different ions must always be coupled with each other. Consequently, the following combination are possible: (i) either oppositely charged ions flow in the same direction; (ii) ions with like charges flow in opposite directions through the reaction product. These simple considerations give the possible limiting cases of a solid state reaction between ionic crystals.

1.2. - INTERFACES

Interfaces play an important role in solid state reactions and, as site of repeatable growth, they can permit equilibrium between point defects to be attained. At

thermodynamic equilibrium, the electrochemical potential across an interface remains constant, but the chemical potentials of the components change because of change in structure. Therefore, electrical charges and discontinuities in electrical potential are observed. A measure of penetration depth of the electrical space charge layer is the so-called Debye-Hückel length:

$$l = \left(\frac{\varepsilon kT}{8\pi n_i e_0^2} \right)^{1/2} \qquad (1\text{-}1)$$

Where ε is the relative dielectric constant, and n_i is the number per cm^3 of univalent particles with positive or negative excess charges in the lattice. If several different sort of mobile particles *i* are present, n_i in the denominator must be replaced by $\sum n_i z_i^2$. The Debye-Hückel length here is taken from the theory of electrolyte solutions. A large number of interfacial phenomena are associated with the electrical surface of interface charge layer.

In order to bring atoms reversibly and isothermally from the undistorted interior of a crystal to an interface an expenditure of free energy is required.

1.3. - TOPOCHEMICAL REACTIONS

Topochemical reactions are solid state reactions under action of a chemical potential gradient that occur essentially at distinguished sites reactant. There are a large number of classical solid state reaction as well as tarnishing reactions in which the morphology of the reaction product is result of the existence of fast transport paths in

which the transport coefficient is relatively high. The morphologies can often be quite unusual and interesting.

Let us consider the formation of spinel in the reaction couple $AO/AB_2O_4/B_2O_3$. It was assumed that the mobility of the oxygen ions is negligible. However, if the reactant oxides AO and B_2O_3 are very porous, then the reaction product AB_2O_4 will also be porous. Furthermore, if the reaction product is an electronic conductor, as is generally the case when the ions A and/or B are transition metal cations, then the oxygen can be transported via the gas phase through the pores, while diffusion of electrons (or electron holes) and ions occur simultaneously in the reaction product.

The reaction rate will then be determined by the diffusion of the faster of the cations, since the transport number of the electronic charge carriers is essentially unity, and, for a sufficiently high porosity, the oxygen gas will always be available everywhere at the reaction front.

Even for compact product layers, gas transport can still occur at a free surface, and this can lead to a unique morphology [7].

Here again, the electronegative component is transported rapidly via the gas phase, while the electrons are transported through the solid, provided that the solid is an electronic conductor. The reaction product can then grow parallel to the surface. The rate of this growth is controlled by the diffusion of the faster cation, since the slower cation is always available for reaction at the three-phase boundary gas/reaction product/reactant. Therefore, as a rule, the overlap of the reaction product at the surface will always occur in the direction towards the reactant containing the slower cation (B

in this case). From the ratio of product layer thicknesses $\Delta x_1/\Delta x_2$, the ratio of the diffusion coefficients of the slower and faster cations can be calculated. If $D_{O^{2-}} << D_{B^{3+}} << D_{A^{2+}}$ in the reaction product, then it follows:

$$\left(\frac{\Delta x_1}{\Delta x_2}\right) \approx \left(\frac{\bar{k}_1}{\bar{k}_2}\right)^{1/2} = \left(8\frac{\overline{D}_B}{\overline{D}_A}\right)^{1/2} \qquad (1\text{-}2)$$

The numerical factor 8 in Eq. (1-2) reflects the fact that the reaction mechanism at the surface and in the interior are different, do that reaction volumes for the passage of one equivalent are not the same in each case.

Surface diffusion can also provide a fast transport path, and than can thus also give rise to rapid growth along the surface.

1.4. - WHY THE FIRST STAGES?

The kinetics and mechanisms of solid state reactions are typically studied making use of mono-dimensional chemical diffusion experiments.

A parabolic rate law is experimentally observed, and this can easily be explained as follows. First of all, we may assume that the local equilibrium occurs at the phase boundaries. This means that, at the phase boundaries, all the thermodynamic variables are fixed, and so the local defect concentrations are also fixed for all time. Therefore, an average concentration gradient of defects is formed in the reaction layer which is inversely proportional to the layer thickness Δx. This results in a flux of ions. The rate-

determining ionic flux is therefore given by $j_i \propto 1/\Delta x$. Since j_i is proportional to the instantaneous growth rate $\Delta x/dt$ of the layer, it follows that $d\Delta x/dt \propto 1/\Delta x$. This expression may be integrated to give the parabolic growth law [8, 9] in the form:

$$\Delta x^2 = 2\bar{k}\,t \qquad (1\text{-}3)$$

Where $\bar{k}$ is known as the practical reaction rate constant.

However, the mechanisms and the kinetics of the interfacial reactions at the first stages (that are, in a sense, the 'true' chemical reactions) are completely unknown, when local chemical equilibrium is not yet obtained [10] and the chemical kinetics is not driven by long range diffusion.

The initial state at an interface between two solid substances with tendency for compound formation is a strong non-equilibrium situation. This is in contrast to later stages of solid-state reactions where compound formation has already be formed, resulting in reduction of the driving forces for subsequent reactions. F. M. d'Heurle [11] and R. Bormann [12] reported that from calculations based on the large driving force available in many systems for first-phase formation is shown that the barrier for nucleation of the first phase is very small, typically the size of the critical nucleus is less than one unit cell. The scientists agree that this very small critical nucleus size indicates that either the application of classical nucleation theory is invalid in this case or that the nucleation site density is so large that the volume fraction associated with nucleation and growth to impingement of the first layer of grains of the product phase is immeasurably small. They suppose that in either case, nucleation should be excluded as a rate-determining factor in the initial reaction between elements and one-dimensional

growth of the product phase in the direction perpendicular to the interface should occur from the very beginning of the reaction.[13-15]

This observation, however, cannot explain some experimental observations. For example, numerous studies of binary systems demonstrated that certain phases are favoured as the first phase, even though the free energies of formation of all the compounds are large enough that anyone could be the first phase. Second, the first phase to form is frequently a metastable phase. The formation of metastable phases requires the presence of barriers, such as interfacial reaction barriers [16, 17] to the formation of the competing equilibrium phases.

From this angle, solid state reaction kinetics (and mechanisms), at the early stages, is (are) the least developed field of chemical kinetics (and mechanisms), in which the gap between theory and experiment seems to be greatest. Introducing the concept of a simple model reaction seems to be a crucial point for further developing the theory towards deeper insight into chemical mechanisms and kinetics at the first stages of solid state reactions, in fact there are currently just few examples of reaction models for solid state reactions at these stages.

The gap between experiments and theory in the early stages of solid state reactions is principally due to the need of an adequate probe to follow these processes (when the equilibrium at the two interfaces is not yet attained as said at the begin of this chapter and the traditional techniques are not applicable [18, 19]) and of a standardized procedure to follow.

An intensive development of Synchrotron Radiation (SR) sources, during the last twenty years, made routine its various applications in chemistry and makes SR techniques really sophisticated and useful tool in the investigation of the early stages of solid state reactions and for the comprehension of all these experimental evidents that cannot be explained with the classical theory , as we'll see more in detail in the next chapters.

It's clear that, once we will be able to fully understand solid state reactions from the early stages, we will be able to control them from the beginning and this important point will make easier the synthesis at the nanoscale and the comprehension of a lot of chemical processes in the solid state (not only for industry but also for basic science).

1.5 - REFERENCES

[1] H. Shmalzried, Solid State Reactions, Verlag Chemie, Wheinheim/Bregstrs. 1974.

[2] M. Soustelle, *Cinétique hétérogène* 3, Ed. Lavoisier - hermès science, Paris, 2006, p. 61-115 ISBn2-7462-1391-5.

[3] FORCERAM editions SEPTIMA, Paris, 1994. Part : J.C NIEPCE et G. THOMAS, *La synthèse par voie solide*, chaptres III-2, pages III—9 à III-68.

[4] M. Cournil and G. Thomas (1979) *J. Thermal Analysis* **17**, 435.

[5] G. Thomas and F. Ropital (1985) *J. Thermal Analysis* **30**, 128.

[6] H. Hauffe, Reaktionen in und an fasten Stoffen, 2nd ed., Springer-Verlag, Berlin 1996.

[7] H. Rickert and C. Wagner (1962) *Ber. Bunsenges. Phys. Chem.* **66**, 502.

[8] G. Valensi (1936) *C.R. Acad. Sci. Paris* **202**,309.

[9] R .E. Carter (1961) *J. Phys. Chem.* **34**, 2010.

[10] G. Thomas and F. Ropital (1983) *J. Thermal Analysis* **28**, 91.

[11] F. M. d'Heurle (1988) *J. Mater. Res.* **3**, 167.

[12] R. Bormann (1994) *Mater. Res. Soc. Symp. Proc.* **343**, 169.

[13] K. R. Coffey, Ph.D. thesis, Massachusetts Institute of Technology, Cambridge, 1989.

[14] D. Ingrain et G. Thomas (1982) *J. Chim. Phys.* **79**, 729.

[15] D. Ingrain et G. Thomas (1983) *J. Chim. Phys.* **80**, 199.

[16] U. Gosele and K. N. Tu (1982) *J. Appl. Phys.* **53**, 3252.

[17] U. Gosele and K. N. Tu (1989) *J. Appl. Phys.* **66**, 2619.

[18] G. Thomas and F. Ropital (1985) *L'Industrie Céramique* **794/5**, 335.

[19] F. Ropital and G. Thomas (1985) *Elsevier Science Publishers, Amsterdam*, 613.

2. THE HAUNT FOR THE REACTION

"Whatever you do will be insignificant,
But is very important that you do it ."

(M. Gandhi)

2.1 - STEP ONE: THE REACTION

Among solid state reactions, the formation of oxide spinels AB_2O_4 is at present the most thoroughly investigated [1-3]: first of all because of the relatively simply crystallographic structure of the spinel. Essentially, it consists of nearly close-packed face-centered-cubic subframe of oxygen ions. There are tetrahedral and octahedral interstices of this subframe that are filled by bivalent and trivalent cations, respectively. In addition, spinels are technically very interesting substances, and one would like to be able to find optimal methods for their preparation. Therefore, the formation of spinels will now be discussed briefly as a classical solid state reaction.

We must first make few assumptions, and under them, it is possible to calculate the rate reaction providing the standard free energy and the component diffusion coefficients of the ions taking part in the reaction: (i) the densities of the reactant oxides AO and B_2O_3 and the reaction product are equal to their theoretical densities and the contact between them is ideal; (ii) in the quasi-binary system AO-B_2O_3 only the spinel AB_2O_4, occurs; (iii) the reaction takes place isothermally; (iv) local thermodynamic equilibrium is maintained within the reaction layer and also at the phase boundaries.

Considering that the transport coefficients of the individual ions are generally rather different from one another and that in spinels the diffusion of oxygen is

negligible, we can eliminate a number of the possible mechanisms. Furthermore, if ideal contact is maintained at the phase boundaries so that the gas phase cannot enter, than the only remaining probable reaction mechanism is the counter-diffusion of cations.

The spinel formation reaction $AO + B_2O_3 \rightarrow AB_2O_4$ is an heterogeneous reaction. Therefore, material must be transported across the phase boundaries and through the reaction product; the resistance to diffusion increases as the thickness of the reaction layer increases. Finally, if the phase boundary resistance can be neglected relative to the diffusional resistance, than local thermodynamic equilibrium will be attained at the phase boundaries. For spinels formation, this state is reached when the reaction layer has attained thickness Δx of the order of 1 μm. Everything we said till now is the theory undergoing the traditional solid state processes for long time of reaction. From this point and for the next chapters in this thesis almost everything is a new and totally unexplored world, from the theory to the experiments used to study this intriguing field that represents the early stages of reaction in the solid state.

2.2 - STEP TWO: THE OXIDE SPINEL

Minerals of the spine1 group, ideally AB_2O_4 oxides of diverse chemistry, are widespread in nature and occur in a number of geological environments including, for example, lunar rocks, and meteorites. In the structure of normal spinel, as mentioned before, the A-site is tetrahedrally coordinated and generally occupied by divalent cations (*e.g.* Mg, Mn, Fe, Ni, Zn). The B-site is octahedrally coordinated and occupied by trivalent cations (*e.g.* Al, Cr, Fe) or in part by tetravalent, such as Ti. Inverse spine1 is characterized by the occupation of one of the B-sites by the divalent cation with one trivalent cation taking its place on the A-site.

A list of some principle oxide spine1s is given in Table 1:

End-Member	Name	Abbr	Ordering
$MgAl_2O_4$	Spinel	Sp	Normal
$MnAl_2O_4$	Galaxite	---	Normal
$FeAl_2O_4$	Hercynite	Hc	Normal
$ZnAl_2O_4$	Gahnite	Gn	Normal
$NiAl_2O_4$	---	---	Inverse

Table 1: Some members of the principle oxide spinels group

As we are looking for a model to study the first stages of the solid state reaction that leads to the formation of spinel it is necessary to take into account some important remarks: (i) it is necessary to have a well known reaction; (ii) the reaction has to lead to a normal spinel, in this case we can neglect the problem of inverse structure and the percentage of the inversion,; (iii) one of the reactant has to permit to be deposited by means of RF-magnetron sputter and the other one has to be purchased in single crystal with a well known orientation (as we will see later); (iv) the reaction conditions have to be mild. Under these assumption, among the oxide spinels reported in Tab. 1, we selected as potential model reaction the one between Al_2O_3 single crystal and MO where M = Mn, Fe and Zn.

Let's consider now the formation of the Mn-Al spinel. First of all we observed, after different deposition attempts, that the stabilization of Mn(II) has been very difficult during the deposition with RF-magnetron sputter and this obliged us to skip to the second candidate.

If we observe the Fe-Al-O system we see a single aluminate based on $FeAl_2O_4$

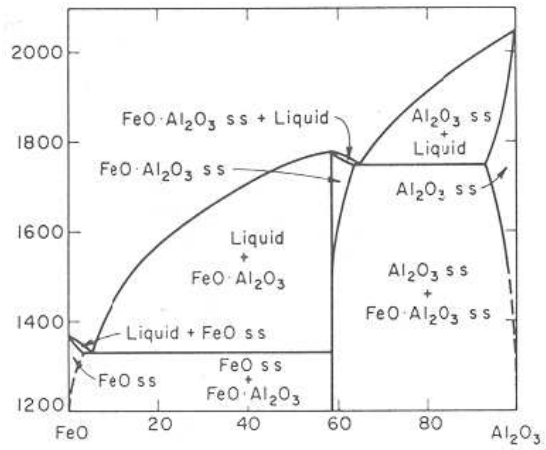

Fig. (2-2): $FeO\text{-}Al_2O_3$ phase diagram

Fisher and Hoffmann [4] showed that the only stable intermediate oxide in the pseudobinary system $FeO\text{-}Al_2O_3$ is $FeAl_2O_4$ (hecynite). The spinel occurs as a continuous series of solid solutions between $FeAl_2O_4$ and Fe_3O_4. Over a narrower range of composition near $FeAl_2O_4$, the spinel equilibrates with "essentially pure Fe" [5,6]. More recently, Meyers *et al.* [7] determined the composition limits of the $FeAl_2O_4$-Fe_2O_3 spinel solid solution equilibrated with $\alpha\text{-}Al_2O_3$ and with FeO (wüstite) as a function of oxygen partial pressure. At lower oxygen partial pressure their results indicate that $\alpha\text{-}Al_2O_3$ equilibrates with the stoichiometric spinel ($FeAl_2O_4$) and essentially pure γ-Fe equilibrates with spinel of increasing Fe:Al ratio with increasing oxygen partial pressure. Below a critical oxygen partial pressure, the spinel is no longer stable and $\alpha\text{-}Al_2O_3$ equilibrates with γ-Fe. The corresponding activity of oxygen in γ-Fe is the critical parameter in predicting spinel formation at internal Fe/$\alpha\text{-}Al_2O_3$ interfaces.

The minimum oxygen concentration in γ-Fe necessary for spinel formation at γ-Fe/$\alpha\text{-}Al_2O_3$ interfaces increases from approximately 1 at. ppm at 1224 K to 20 at. ppm at 1623 K. Over this temperature range the threshold oxygen level increases from

approximately 1/10 to 1/5 of the solubility limit of oxygen in γ-Fe in equilibrium of wüstite. What we can observe from all these data and information is that the conditions to stabilized Fe-Al spinel are very difficult to achieve.

Among the three selected oxide spinels (*i.e.* $ZnAl_2O_4$, $MnAl_2O_4$ and $FeAl_2O_4$), in conclusion, we selected the couple of parent oxides that leads to a single product, that is Al_2O_3-ZnO, according to the phase diagram.

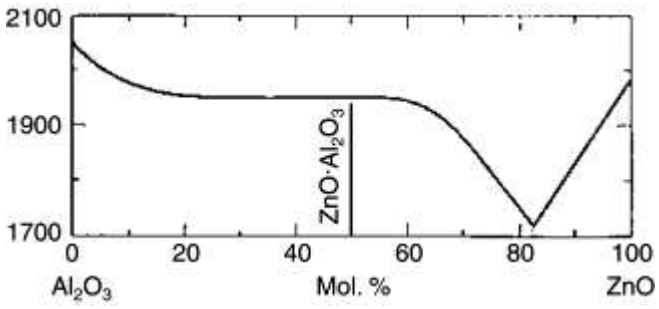

Fig. (2.3) – Phase diagram for the couple of parent oxides α-Al_2O_3\ZnO

We choose this couple of parent oxides taking into account that the presence of just one reaction product is a crucial point for the model, in this way we can neglect the variable dues to the presence of different products at different reaction extent and be sure that the only one is the Zn-Al spinel. In addition, ZnO is a very important material in electronic and spintronic fields. A quite large number of topotactical relationships can be found at the interface between ZnO and Al_2O_3 [8 and references there in] single crystals.

Zinc oxide (ZnO) films are a wide band gap II–VI semiconductors, so they are very useful in light emitting diodes and surface acoustic wave devices. Differences of electron mobility and in the topotactical relationships in ZnO films grown on the

various orientations of sapphire single crystals, have been reported, but there are no systematic studies on the ZnO || Al_2O_3 interfaces.

To perform the reaction we used Al_2O_3 single crystals with three different orientations, with the aim to study the mechanism and the kinetic of the process also as a function of the topochemical relationships; the other oxide was powder ZnO that we deposited as a very thin films onto the alumina crystals, as we'll see more in detail in the next section.

It's obvious that, once the model and the analysis strategy will be build up, than it will be possible to apply the criterion, with the necessary little modifications, at a lot of solid state reactions and not only to these that concern spinels formation.

2.3 - THE IDEA

As we said in previous chapter, when we speak about the early stages of solid state reactions we consider that the local chemical equilibrium is not yet attained at the interfaces and that, in these conditions, we have not an adequate probe and model.

It has been demonstrated by our group [9, 10] that insight about mechanism and kinetic at these very early stages can be obtained by performing the reaction using at least one of the two reactants in form of very thin film (10 ÷ 20 nm) and using a local probe for the local chemical environment of one of the constituent.

The approach towards the reactivity in the solid state is primarily based on recognizing the crucial role played by the interfacial free energy and by the topotactical

relationship between the two reactants, which in turn control formation of the new phase and its spatial and orientational relationships with respect the parent phases. Using one of the reactants in form of film, and considering films of different thicknesses, the ratio between bulk and interfacial free energy can be changed, and the effect of interfacial free energy can be maximized (by using the reactant in form of thin film) and finely tuned. So, it is possible to switch from a situation where the interfacial contribution is the largest to another where bulk contribution rules the process, that is from a quasi–2D to a 3D reactive system. Three different regimes can be explored and clarified.

a) For very thin films, the reactive system is quasi-2D, the interfacial term dominates the overall free energy, and different products can be thermodynamically stabilised by the interfacial free energy: for given structures and compositions, the effect is controlled by the topotactical relationships and is different for different interfaces.

b) For intermediate thickness, once the final phase has nucleated, interfacial movement is the rate-determining step: topotaxy and interfacial free energy control the rate of the reaction.

c) For thick reaction layers, diffusion is the rate-determining step and the interfacial term is negligible.

We expect that the transitions between the regimes could be directed towards different products and investigated by changing the dimensionality of the reactive couple. To the best of our knowledge, this approach towards the reactivity in the solid state is completely original.

The strategy that it has been then performed consists in the use of a lot of different techniques, most of them depending on synchrotron radiation. The principal stages of the strategy of investigation are:

1) The construction of the model, by means of deposition of very thin films of MO (M = divalent metal) on a substrate, that is a single crystal
2) The firing at different temperature and for different amount of time, to carry out the reaction and to have the samples at different extent of reaction
3) The use of M-k edge (where M is the divalent metal) fluo-XAS (but it's possible to use also refl-EXAFS, depending on the sample) to observe the local environment of the metal
4) The use of M-k edge micro-XANES to have a sort of map of concentration of one of the constituent (that give data that are comparable to those of SIMS)
5) The use of surface and classical diffractions
6) The use of AFM to explore the surface changes that may occur during the reaction

In next chapters and sections we'll analyze in detail every single point of the strategy we have planned now.

2.4 - REFERENCES

[1] H. Hauffe, Reaktionen in und an fasten Stoffen, 2nd ed., Springer-Verlag, Berlin 1996.

[2] H. Shmalzried (1965) *Ber. Dtsch. Keram. Ges* **42**, 11.

[3] J. S. Armijo (1969) *J. Oxidation of Metals* **1,** 171.

[4] W. A. Fisher and A. Hoffmann (1956) *Arch. Eisenhüttenwes,* **27**, 343.

[5] L. M. Atlas and W. K. Sumida (1958) *J. Am. Chem. Soc.* **41**, 150.

[6] N. G. Schmahl and H. Dillenburg (1969) *Z. Physik. Chem. N. F.* **65**, 119.

[7] C. E. Meyers, T. O. Mason, W. T. Petuskey, J. W. Halloran and H. K. Bowen (1980) *J. Am. Chem. Soc.* **63**, 659.

[8] S.-H. Lim, D. Shindo, H-. B Kang and K, Nakamura (2001) *J. Cryst. Growth* **225,** 202.

[9] F. D'Acapito, P. Ghigna, I. Alessandri, A. Cardelli, I. Davoli (2003) *Nucl. Instrum. Methods Phys. Res. B* **200**, 421.

[10] P. Ghigna, G. Spinolo, I. Alessandri, I. Davoli, F. D'Acapito (2003) *Phys. Chem. Chem. Phys.* **5** 2244.

3. A MODEL TO EXPLORE EXPERIMENTS AND THEORY

"Whenever a theory appears to you as the only possible one, take this as a sign that you have neither understood the theory nor the problem which it was intended to solve ."

(K. Popper)

3.1 - BUILDING UP THE FIRST STAGES OF THE MODEL

As we said in previous chapters, when we speak about the early stages of solid state reactions we consider that the local chemical equilibrium is not yet attained at the interfaces and that, in these conditions, we have not an adequate probe and model.

It has been demonstrated by our group [1, 2] that insight about mechanism and kinetics at these very early stages can be obtained by: (i) performing the reaction using at least one of the two reactants in form of very thin film (10 ÷ 20 nm); (ii) using a local probe for the local chemical environment of one of the constituent.

In this section we will explore the experimental procedure that we use to prepare the model to simulate the early stages of the solid state reactions.

After the choice of the two parent oxides, as described in the previous chapter and taking into account all the previous assumptions, we will describe the experimental procedure that it has been carried out for the model preparation. Zinc oxide films were deposited by a RF-magnetron sputtering using a zinc oxide target. The deposition conditions were optimized to give good quality films suitable for the study of the interfaces and of the first stages of solid state reactions.

3.2 - ZnO THIN FILMS DEPOSITION

Zinc oxide (ZnO) films are a wide band gap (3.37 eV) II–VI semiconductor, which has a large electro-mechanical coupling factor, high piezoelectric coefficient, photoconductivity, and is transparent in the visible and infrared ranges, so they are very useful in light emitting diodes and surface acoustic wave devices [3]. However, the optical and electrical properties of epitaxial films [4,5] are critically dependent on the defects and interface structure. Srikant *et al.* [6] reported on the differences of electron mobility in ZnO films grown on the various orientations of sapphire. These properties are attributed to the differences of dislocation density in the films produced as a result of the different lattice mismatches, as a consequence of different orientations of the sapphire. Therefore, it is very important to clarify the interface structure in order to have a full understanding of the epitaxial growth and properties of ZnO films.

Since the lattice mismatch between the ZnO films and the sapphire is low, it is expected that high quality ZnO films on the sapphire will be achieved.

ZnO films can be deposited by a variety of deposition techniques based on the specific applications one needs from these films. Epitaxial ZnO films were grown on sapphire substrates by chemical vapor deposition (CVD) [7]. Recently pulse laser deposition has been tried to deposit ZnO films. By the way, the most common technique to deposit ZnO films, and the one we used, is by sputtering technique. Both DC and RF. sputtering techniques can be used to deposit ZnO films [8-11]. The resistivity of the deposited ZnO films depends on the sputtering conditions. Usually, the films deposited without oxygen in the sputtering ambient are non-stoichiometric with conducting nature. This is due to the overstoichiometry of Zn in the deposited films [12].

In the present work, as we said, ZnO films were deposited by an RF-magnetron sputtering technique using ZnO target. The deposition conditions were optimized according to Sundaram *et al.,* except for the deposition temperature, because after our preliminary tests it has been observed that on very thin films it's better to conduct the deposition at room temperature [13]. In fact, as we'll discuss later, using the deposition conditions reported by Sundaram, we observed that for very thin films at 250 °C we have an initial reaction at the surface. In Fig. (3-1) the XRPD spectra of ZnO reference and ZnO thin film deposited at 250 °C onto Al_2O_3 $(11\bar{2}0)$ as a preliminary test, are reported.

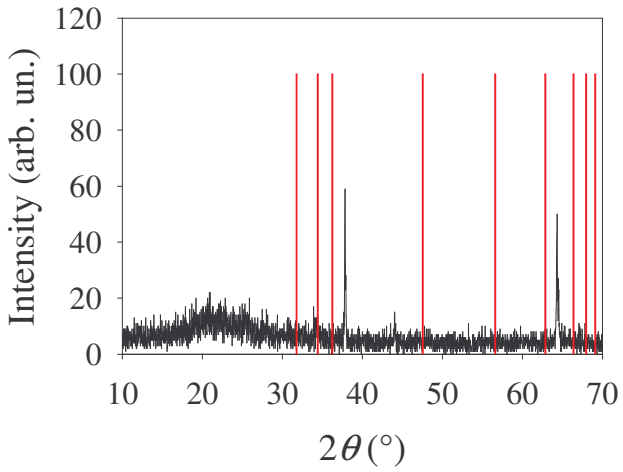

Fig. (3-1): XRPD spectrum of the ZnO thin film deposited at 250 °C onto Al_2O_3 $(11\bar{2}0)$, according to Sundaram *et al.* (black line). For comparison purposes the ZnO reference lines are reported (red bars)

The ZnO films were deposited by means of a RF-magnetron sputter using a 5 cm diameter by 0.625 cm thick ZnO target (99.999% purity, Sigma-Aldrich). Alumina single square crystals with different orientations, (0001), $(1\bar{1}02)$ and $(11\bar{2}0)$, one side polished (MaTeck) were used as substrates. The substrates were thoroughly cleaned with organic solvent, dried before loading in the sputtering system and placed in the stainless steel substrate holder. The temperature of the substrate was monitored with

thermocouple attached near the substrate. The system was evacuated to a vacuum of the order of 10^{-5} bar using in a first step a mechanical pump and then a turbo pump. The deposition has been carried out at ambient temperature.

The argon/oxygen gas injection was achieved through a shower head-like stainless steel tubing with a number of small opening. The ratio of argon (99.99% purity) and oxygen (99.99% purity) were dialled in the electronic mass flow meters. The gases were mixed before entering the chamber and were allowed to flow through an inlet valve to the chamber. Once the desired vacuum was achieved, a throttle valve was used to adjust the chamber pressure during sputtering. Once the plasma was struck, the pressure and the power were adjusted to the desired conditions. The reflected power was tuned to a minimum value and some times it was necessary to increase the forward power to achieve minimum condition. The substrate was then rotated to place above the target and the deposition was initiated. Table 2 reported a summary of the deposition conditions:

Substrate temperature (°C)	25
Target – substrate distance (cm)	3
Oxygen / Argon flow ratio	2 : 3
Pressure during sputtering (bar)	1×10^{-5}
Forward power (W)	60
Reflected power (W)	0
Deposition time (minutes)	10
Thickness (nm)	13

Table 2: Conditions for the sputtering process for samples preparation

The thickness of the deposited films were measured using a Bruker X-ray Diffractometer (model D8), Cu $K\alpha$ = 1.54 Å, by means of the Debye-Sherrer equation:

$$t = \frac{K\lambda}{B\cos\theta_B} \qquad (2\text{-}1)$$

Here t is the mean crystallite dimension; K is a dimensionless constant that may range from 0.89 to 1.39 depending on the specific geometry of the scattering objects. For a perfect two-dimensional lattice, where every point on the lattice emits a spherical wave, numerical calculations yield the lower bound of 0.89 for K [17]; λ is the x-ray wavelength (for a Cu-source is 1.54 Å); B is the line broadening at half maximum intensity (FWHM) in radians and θ_B is the Brag angle.

Studies of the deposited films were then performed using the Atomic Force Microscope (SPM, SPEECO) and Linear Dichroism measurements, that have been carried out at the GILDA BM08 beamline of the European Synchrotron Radiation Facilities (E.S.R.F.) in Grenoble (FR) (Exp CH-2427).

Once the films have been deposited, an annealing procedure have been done. The interfaces have been fired, in air, at 600 °C for 20 minutes. The same treatments have been conduced on all the three systems.

All the interfaces are than cooled down and observed by means of different techniques, both with synchrotron radiation and classical.

Let's start to consider the X-Ray Diffraction (XRPD) analysis. Fig. (3-2) shows the diffraction patterns of the films deposited on sapphire substrates for the different orientations deposited at 25°C onto Al_2O_3 $(11\bar{2}0)$, for comparison the ZnO references are reported.

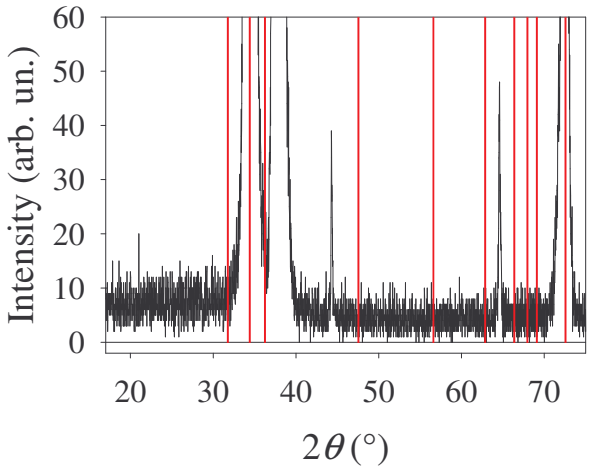

Fig. (3-2): XRPD spectrum of the ZnO thin film deposited at 25 °C onto Al_2O_3 $(11\bar{2}0)$ (black line). For comparison purposes the ZnO reference lines are reported (red bars)

What we can observe by looking at the XRPD spectrum and looking also at Fig. (3-1) is that, as we said before, at 250 °C the deposited film is not ZnO. May be because, in a very thin film a sort of reaction takes place on the alumina substrate during the deposition, just after the first deposition of the first ions from the target. In fact, if we look at the peaks of both the films compared to the standard powder it's clearly visible that the peaks corresponding to the ZnO are no visible at 250 °C while some other peaks appear. We had no conduct deeper analysis on them because our priority was the ZnO thin film deposition. After these insights we decided to change the deposition conditions. The same observations are for the three studied interfaces.

From the XRPD spectra at 25 °C we observe only two peaks identified by comparison with JCPDS file 03-0891 (International Center for Diffraction Data, 1990). The peaks that are seen are at 34.4 ° and 72.6° and they are equivalent to d-spacings of 0.2603 and 0.1302 nm corresponding to (002) and (004) plane reflections from hexagonal type ZnO with a = 0.32498 and c = 0.52066 nm.

Another important characteristic is that it's possible to observe that the deposited films onto the sapphire single crystals have different behaviour depending on the substrate orientation, in fact, a huge dichroic effect is very well visible just after the deposition. Fig. (3-3) shows the Zn-K edge X-ray Absorption Near Edge Spectroscopy (XANES) spectra of ZnO deposited onto the three sapphire orientations.

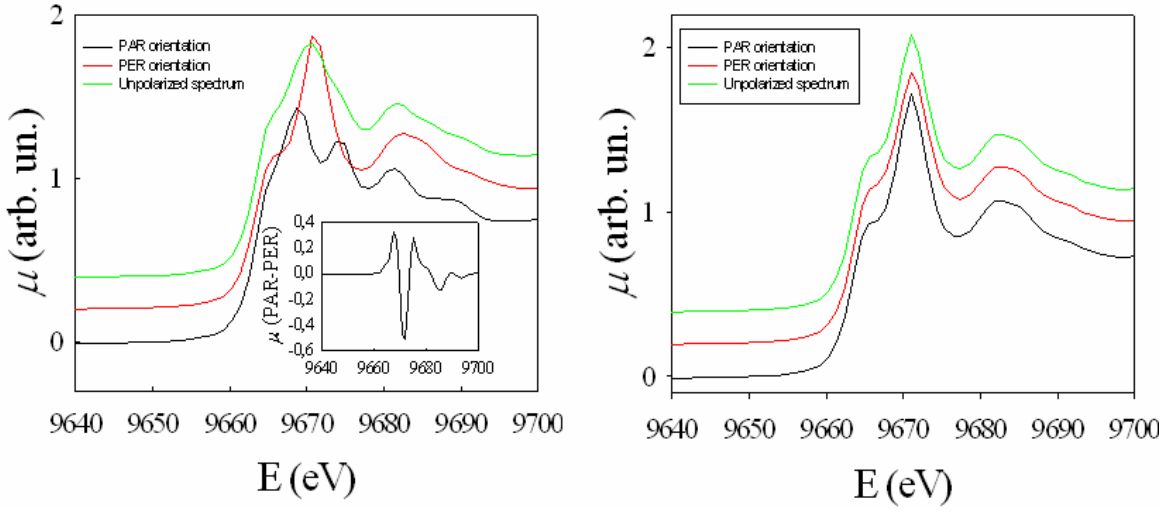

Fig. (3-3): Zn-K edge XANES. The left figure refers to the reactive interfaces $(0001)_{ZnO} \parallel (11\bar{2}0)_{sapphire}$ and $(0001)_{ZnO} \parallel (0001)_{sapphire}$ where a huge linear dichroic effect is very well visible. The right figure refers to the reactive interface $(11\bar{2}0)_{ZnO} \parallel (1\bar{1}02)_{sapphire}$ where no linear dichroic is found. For comparison purposes the unpolarized spectra are reported.

The Zn-K edge XANES spectra are collected, for each substrate, with the two different orientations of the electric field of the beam with respect to the sample surface, parallel (PAR) and perpendicular (PER). The unpolarized spectra, obtained using the

Stokes parameters for the calculations, are also shown for reference. The linear dichroism, defined as the difference between the spectrum collected with the electric field parallel and perpendicular (PAR–PER) to the sample surface is also shown.

Analyzing these spectra it's clear that the difference between the films deposited onto Al_2O_3 $(11\bar{2}0)$, (0001) and the one deposited onto Al_2O_3 $(1\bar{1}02)$. In fact, even if the films have been deposited all under same conditions a huge dichroic effect on the two first orientations (while no effect on the last one), it's visible.

Comparison with literature data at the Zn–K edge for a wurtzite single crystal and films [18, 19] shows that the ZnO film is highly oriented if not single crystal. In particular, for the first two orientations, it should be noted that our XANES manifold for the PAR(PER) electric field of the beam corresponds to that of a highly oriented wurtzite film [19] with the *c* axis perpendicular to the film surface for the PER(PAR)orientation: therefore in our case the *c* axis is parallel to the film surface. The topotactic relationship between the ZnO film and sapphire are $(11\bar{2}0)_{ZnO} \parallel (1\bar{1}02)_{sapphire}$ and $[0001]_{ZnO} \parallel (1\bar{1}01)_{sapphire}$, as already observed by Lim *et al.* [9] and Ay *et al.* [20]. The same comparison shows that the film deposited onto the $(11\bar{2}0)$ and (0001) Al_2O_3 single crystals is found with the *c* axis of wurtzite perpendicular to the film surface. The topotactic relationships between ZnO film and sapphire are therefore $(0001)_{ZnO} \parallel (11\bar{2}0)_{sapphire}$ and $(0001)_{ZnO} \parallel (0001)_{sapphire}$, again in agreement with previous works [9, 20]. For the film deposited onto the third orientation we can say that it is polycrystalline.

The film morphology, observed by means of AFM (for better details, see Chapter 7) after the deposition and the anneal is extremely regular and without a strong roughness taht has been measured and evaluated to be meanly 20 nm, for all the three orientations of the substrates (as we can observe in Fig. (3-4)).

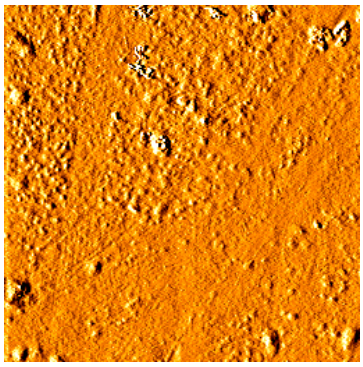

Fig. (3-4): AFM image of the substrate after ZnO deposition and anneal at 600 °C in air.

After this first analysis, the sample have been treated for different temperatures at different amount of time. The procedure, has been chosen taking into account that for temperatures higher than 800 °C we have the evaporation of ZnO. After a series of preliminary tests we treated the samples as indicated in Table 3:

Heating temperature (°C)	**Time (minutes)**
25	---
200	20
300	20
400	20
600	20
800	20
800	40
800	60
800	120

Table 3: Conditions used for the samples reaction

3.3 - REFERENCES

[1] F. D'Acapito, P. Ghigna, I. Alessandri, A. Cardelli, I. Davoli (2003) *Nucl. Instrum. Methods Phys. Res. B* **200**, 421.

[2] P. Ghigna, G. Spinolo, I. Alessandri, I. Davoli, F. D'Acapito (2003) *Phys. Chem. Chem. Phys.* **5** 2244.

[3] R.F. Service (1997) *Science* **276,** 895.

[4] D. J. Eaglesham, D. M. Maher, E. P. Kvam, J. C. Bean and C. J. Humphreys (1989) *Phys. Rev. Lett.* **62**, 187.

[5] F. Ernst, P. Pirouz and A.H. Heuer (1991) *Phil. Mag. A* **63**, 259.

[6] V. Srikant and D. R. Clarke (1997) *J. Appl. Phys.* **81**, 6357.

[7] A. Plzzmx, N. Butta, D. Narduccl and M. Palladino (1989) *J. Electrochem Soc.* **136,** 1945.

[8] S. Manxv and A. Zangvd (1978) *J Appl. Phys* **49,** 2787.

[9] V. Cracmn, J. Elders, J.G. E. Gardemers and I. W. Boyd (1994) *Appl. Phys. Lett.* **65** 296.

[10] T. Hada, K. Wasa and S. Hayakawa (1971) *Thin Solid Films* **7***,* 135.

[11] R. J. Lad, P. D. Funkenbusch and C. R. Aita (1980) *Or. Vac. Sct. Technol* **17,** 808.

[12] G. A. Rozgonyx and W. J. Pohto (1966) *Appl Phys Lett.* **8***,* 220.

[13] K. B. Sundaram and A. Khan (1997) *Thin Solid Films* **295,** 87.

4. G.I.L.D.A. - BM08 AT E.S.R.F. AND THE FLUORESCENCE-XAS

"Science may set limits to knowledge, but should not set limits to imagination."

(B. Russel)

4.1 - XAS AND FLUO-XAS: WHO ARE THEM?

The advent of synchrotron radiation sources made possible to exploit the fine structure of the absorption coefficient (XAFS) to get information on both the local geometric and electronic structure of matter.

Let us concentrate on *absorption spectroscopy*. When the X-ray photon energy increases, the absorption coefficient μ progressively decreases. This smooth behaviour is interrupted by sharp discontinuities, the *absorption edges*, which originate when the photon energy becomes high enough to extract an electron from a core level.

In correspondence of an edge, the absorption coefficient exhibits the X-ray Absorption Fine Structure (XAFS).

XAFS is customarily divided into two regions.

a) The structure within 30÷50 eV above the edge is called XANES (X-ray Absorption Near Edge Structure), and we will discuss it in Chap. 5

b) The fine structure extending from the XANES region up to typically one thousand eV is called EXAFS (Extended X-ray Absorption Fine structure). EXAFS carries information on the local structure surrounding a given atomic species.

When an X-ray photon of high enough energy is absorbed by an atom, a core electron is ejected from the atom. The kinetic energy of the photo-electron is the difference between the photon energy and the core binding energy. The outgoing photo-electron is described by a spherical wave, whose wavelength decreases when the photon energy increases. If the absorber atom is not isolated, the photo-electron can be back-scattered by neighbouring atoms, giving rise to an incoming spherical wave. The absorption coefficient μ depends, to first order, on the dipole matrix element between the initial core state φ_i and the photo-electron final state φ_f, which in turn is superposition of the outgoing and incoming spherical waves. The phase relationship between outgoing and incoming waves depends on the photo-electron wavelength and inter-atomic distance R. The variation of phase relationship as a function of photon energy influences the final state amplitude at the core site, giving rise to an interference phenomenon which modulates the absorption coefficient. The frequency of EXAFS oscillation depends on the distance between absorber and back-scatterer atoms. Their amplitude is proportional to the number of back-scatterer atoms.

Two main peculiarities characterize EXAFS: (i) the selectivity to atomic species, which is achieved by tuning the X-ray energy to the corresponding absorption edge; (ii) the insensitivity long-range order, due to the short mean free path of the photo-electron, typically limited to about 10 Å.

An atom, excited or ionized by absorption of an X-ray photon, contains a core hole. This configuration is unstable, and the atom spontaneously tends to relax, filling the core hole with an electron from an upper level and thereby reducing its energy. Two types of de-excitation are possible.

a) Radiative de-excitation (or fluorescence), that is our case. The available energy is emitted as an X-ray photon. The energies of fluorescence photons depend on the species. Fluorescence X-ray characteristic emission lines univocally identify the atom species.

b) Non radiative de-excitation (or Auger effect). The available energy is used to eject a second electron from an upper level.

The two de-excitation mechanisms are in competition. The fluorescence yields depends on the atomic number

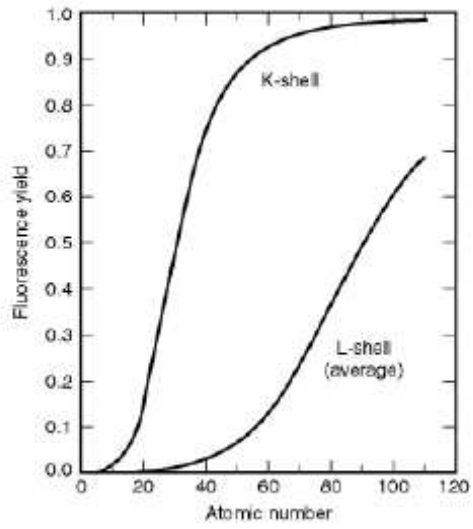

Fig. (4-1): Fluorescence yield for K and L shells. The plotted curve for L shells represents an average of L1, L2 and L3 effective yields. This figure is taken from the X-ray data booklet web site: **http://xdb.lbl.gov**

The total de-excitation probability per unit time determines the core-hole lifetime. The deeper the core hole and the larger the atomic number *Z*, the larger is the number of upper levels from which an electron can drop to fill the core hole and consequently the shorter is the core hole lifetime τ_h (typically $10^{-15} \div 10^{-16}$ seconds).

These peculiarities make EXAFS a very appealing local structural probe.

4.2 - THE EXAFS EQUATION

In a non-isolated system, the photo-electron can interact with the surrounding atoms and undergo scattering. In the EXAFS region the photo-electron energy is much larger than electron-atom interaction energy, so that the interaction causes a weak perturbation to the final state:

$$\left|\varphi_f\right\rangle = \left|\varphi_f^0 + \delta\varphi_f\right\rangle \qquad (4\text{-}1)$$

And the absorption coefficient becomes:

$$\mu(\omega) \propto \left|\left\langle \varphi_i \left| \hat{\eta}\cdot\bar{r} \right| \varphi_f^0 + \delta\varphi_f \right\rangle\right|^2 \qquad (4\text{-}2)$$

The perturbation $\delta\varphi_f$ corresponds phenomenologically to an incoming spherical wave.

EXAFS is defined as the difference between the actual absorption coefficient μ and the atomic absorption coefficient μ_0, normalized to $\Delta\mu_0$:

$$\chi(k) = (\mu - \mu_0)/\Delta\mu_0 \qquad (4\text{-}3)$$

And is generally expressed as a function of the photoelectron wave-number k rather then energy.

Let us consider an ideal system composed by atoms frozen at their equilibrium position.

The simplest system consists of two atoms, an absorber one *A* and a back-scatterer one *B*; let $\mathbf{R}_B$ be the vector joining the two atomic positions. The potential experienced by the photo-electron is rather complicated. In general, one relies on the muffin tin approximation. Using a series of calculation that are too far from this simple theoretical section and consider a series of approximation, such as the small atom approximation and the plane wave approximation, Eq. (4-4) is found:

$$\chi(k) = \left(1/kR_B^2\right)\left| f_B(k,\pi)\right| \sin[2kR_B + \phi(k)] \qquad (4\text{-}4)$$

Basically, the EXAFS signal has a sinusoidal behavior, with frequency $2R_B$ proportional to the inter-atomic distance. The phase of the sine function is perturbed by the phase-shift $\phi(k)$, while the amplitude is modulated $|f_B(k, \pi)|$.

Let us consider now a system composed by any number of atoms. The generalization of Eq. (4-4) is immediate, so long as the possibility of multiple scattering of the photo-electron by several atoms is negligible. Within the single scattering atom approximation, the EXAFS function can be built up as the sum of many two-atomic contribution. Let $\mathbf{R}_j$ be the vector position of the *j*-th atom with respect to the absorber atom:

$$\chi(k) = (1/k)\sum_j (1/R_j^2)\,\mathrm{Im}\left\{f_j(k,\pi)e^{2i\delta_1}e^{2ikR_j}\right\} \qquad (4\text{-}5)$$

The treatment we have done till now does not take into account inelastic effects, that are of two types: (i) Intrinsic inelastic effects and (ii) extrinsic inelastic effects. Taking them into account we arrive at Eq. (4-6):

$$\chi(k) = (S_0^2 / k)\sum_j (e^{-2R_j/\lambda} / R_j^2)\,\mathrm{Im}\left\{f_j(k,\pi)e^{2i\delta_1}e^{2ikR_j}\right\} \qquad (4\text{-}6)$$

If atoms can be grouped into coordination shells, each one containing N_s atoms of the same species at the same distance R_s from the absorber atom, it is convenient to separate the contribution of different coordination shell (Eq. (4-7)):

$$\chi(k) = (S_0^2 / k)\sum_s N_s\,\mathrm{Im}\left\{f_s(k,\pi)e^{2i\delta_1}(e^{-2R_s/\lambda} / R_s^2)e^{2ikR_s}\right\} \qquad (4\text{-}7)$$

Here, the parameter N_s is the coordination number of the shell *s*.

Every real physical system is then affected by thermal disorder (due to the thermal motion of atoms) and by structural disorder. The EXAFS equation for one coordination shell becomes Eq.(4-8):

$$\chi_s(k) = (S_0^2 / k)N_s\,\mathrm{Im}\left\{f_s(k,\pi)e^{2i\delta_1}\int \rho(r)(e^{-2r/\lambda} / r^2)e^{2ikr}dr\right\} \qquad (4\text{-}8)$$

It's important to observe that this equation is the Fourier Transform of the function $\rho(r)$.

The fundamental problem of EXAFS analysis is to recover the distribution $\rho(r)$ from the experimental spectrum $\chi(k)$. No exact solution can be given to this problem,

because every experimental spectrum has a finite extension, within the values k_{min} and k_{max}. In particular, for $k_{min} \leq 2 \div 3 Å^{-1}$ the EXAFS signal cannot generally be utilized because of difficulty in determining the atomic absorption coefficient μ_0 in the vicinity of the edge, effects of the core-hole lifetime on the low-energy electrons and influence of multiple scattering processes.

An approximate solution to the inversion problem from $\chi(k)$ to $\rho(r)$ consists in hypothesizing physically sound structural models and in fitting the parameters of their distributions $\rho(r)$ to the experimental EXAFS spectrum.

Taking into account all these assumptions the standard formula is found (Eq. (4-9)):

$$\chi(k) = \sum_j \frac{N_j f_j(k) e^{-2R_j/\lambda(k)} e^{-2k^2\sigma_j^2}}{kR_j^2} \sin\left[2kR_j + \delta_j(k)\right] \qquad (4\text{-}9)$$

By using Eq. (4-9) one can get from EXAFS information on the local structure.

i) Coordination number: amplitude of the EXAFS signal is directly proportional to the number N of the atoms in the shell

ii) Inter-atomic distance: frequency of the EXAFS signal depends on the averaged inter-atomic distance

iii) Debye-Waller factor: mean square relative displacement of absorber and back-scatterer atoms

4.3 - THE EXPERIMENTAL TECHNIQUE

As we said before, the EXAFS technique requires the measurement of the X-ray absorption coefficient as a function of photon energy. The standard experimental set-up for this kind of analysis is generally composed by: (i) an optical apparatus, containing a monochromator and one or more X-ray mirrors; (ii) a measurement apparatus, containing sample holders and detectors for measuring the absorption coefficient.

Different instrumental configurations allow to measure μ. Let us present here the one we used for our samples: the fluo-EXAFS set-up.

When the absorbing species *A* is a tiny fraction of the entire sample, its contribution μ_A to the total absorption coefficient μ_{tot} is small. For concentrations typically lower than 1%, XAFS structures of μ_A are comparable to the statistical noise of μ_{tot}. In this case transmission measurements are ineffective.

In general, for diluted samples one uses fluorescence measurements, in which the intensity I_f of the fluorescence emitted at frequency ω_f by the absorbing species *A,* as a result of radiative de-excitation, is measured as a function of incident energy $\hbar\omega$. For a thick sample, in the simplifying hypothesis that both the impinging beam (I_0) and the fluorescence beam (I_f) make an angle of 45° with the sample surface, one can show that

$$I_f(\omega) = I_0(\omega)(\Omega/4\pi)\eta\mu_A(\omega)/[\mu_{tot}(\omega) + \mu_{tot}(\omega_f)] \qquad (4\text{-}10)$$

According to Eq. (4-10), the fluorescence intensity I_f: (i) is proportional to the impinging flux I_0; (ii) is proportional to the solid angle $\Omega/4\pi$ determined by the detector

acceptance; (iii) is proportional to the fluorescence yield η; (iv) depends on the fraction μ_A/μ_{tot} of impinging beam which is absorbed by the *A* species, and on the subsequent absorption of the fluorescence radiation ω_f from the whole sample. The fluorescence intensity I_f is to a good approximation proportional to μA only when μA << μtot, say for very diluted samples. For thick non diluted samples fluorescence measurements give rise to distortion in the EXAFS amplitude.

4.4 - FIT STRATEGY

The EXAFS data analysis is carried out trough different steps:

(i) Extraction of the EXAFS signal

The first step of the data analysis consists in extracting the contribution μx of the edge of the selected element from the experimental signal:

$$\mu x = \ln(\frac{I_0}{I}) - \mu_n x \qquad (4\text{-}11)$$

Where μ_n is the contribution of all the other excitations of the selected element plus the excitations of the other elements of the compound. In the pre-edge energy region, $\mu_n x = \ln(I_0/I)$. Above the edge energy μ_n is estimated by extrapolating the pre-edge behavior.

The threshold energy is arbitrarily chosen in correspondence of some characteristic point of the edge, for example the first inflection point.

The atomic absorption coefficient μ_0 has now to be known, in order to calculate the EXAFS function $\chi(k) = (\mu - \mu_0)/\Delta\mu_0$ (Eq. 4-12). To evaluate μ_0 one looks for a

curve which averages the oscillations of the absorption coefficient. A frequently utilized approach is based on polynomial splines. This step of the analysis is generally made by a trial and error procedure, and requires patience and skillfulness.

(ii) Fourier filtering

The first step of Fourier filtering is the direct transform from *k* to *r* space:

$$F(r) = \int_{k_{\min}}^{k_{\max}} \chi(k) W(k) k^n e^{2ikr} dk \qquad (4\text{-}13)$$

Where *W(k)* is a window function which reduces the spurious oscillations induced by the finite *k* range. The term k^n is used to balance the low- and high-*k* parts of the spectrum (typically n=1÷3). The integral limits k_{min} and k_{max} are chosen so as to exclude both the low-*k* signal, where the EXAFS formula is unreliable (typically k_{min} > 2 ÷ 4 $Å^{-1}$), and the high-*k* signal, where the signal to noise ratio is small.

By means of EXAFS in fluorescence mode we plan to observe the product that are formed at the three reactive interfaces and collecting the spectra step by step, that is after each thermal treatment described in Chapter 2 (observing and analyzing all the product that are formed) we plan to obtain some insights on the reaction mechanism. Once we have obtained such kind of information, we would to try to give a kinetic description of the mechanism that describe the formation of the final product.

4.5 - EXPERIMENTAL PART

Fluorescence-XAFS spectra were collected at the GILDA BM08 beamline [1] at the ESRF (European Synchrotron Radiation Facility) at the Zn-K edge (Exp. CH-2427). The device uses a 0.8 T Bending Magnet (BM) source operating at 6 GeV with typical currents of 200 mA. The characteristics of the beam-line are a high resolution ($\Delta E / E \sim 10^{-4}$), a high flux ($\sim 10^{11}$ph/s) and a few millimetre spot size (typically $1 \times 1 mm^2$) on the sample. The energy range of operation is 5 – 80 keV.

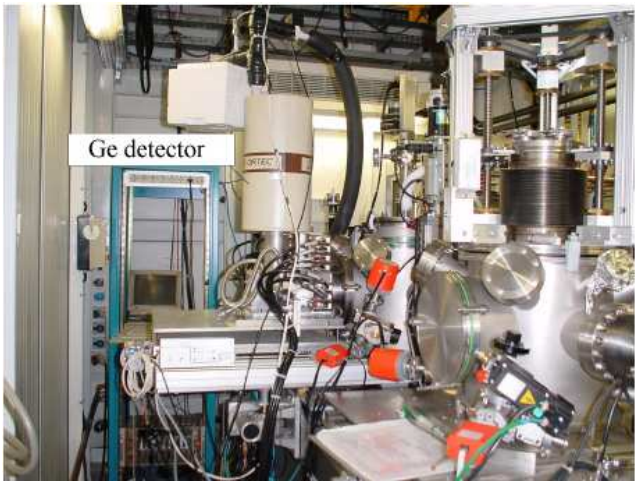

Fig (4-1): Experimental chamber with HPGe solid state detector

A Si (311) double crystal monochromator was used; the harmonic rejection was realized by Pd mirrors, having a cut-off energy of 20 keV. A 13-elements high purity germanium detector was used for the collection of the fluorescence spectra, with the sample at 14.5° (84.5°) with respect to the incoming beam (that is the radiation electric field parallel(perpendicular) PAR(PER) to the sample surface orientation). Unpolarized spectra have been obtained by averaging the spectra taken with the two different polarizations using the Stokes parameters. The measurements were performed at room temperature. To obtain a reasonable signal to noise ratio, the integration time was adjusted to give $\cong 10^6$ counts in the fluorescence channel; in addition, in order to avoid

distortions of the spectra, the count rate of each element was kept well below the saturation limit.

In Fig. (4-2) is shown, as an example, the raw fluorescence data at the Zn–K edge for a ZnO film deposited onto a $(1\,\bar{1}\,0\,2)$ Al_2O_3 single crystal and heated at 600 °C for 20 minutes: for this spectrum the electrical field vector is perpendicular to the sample surface.

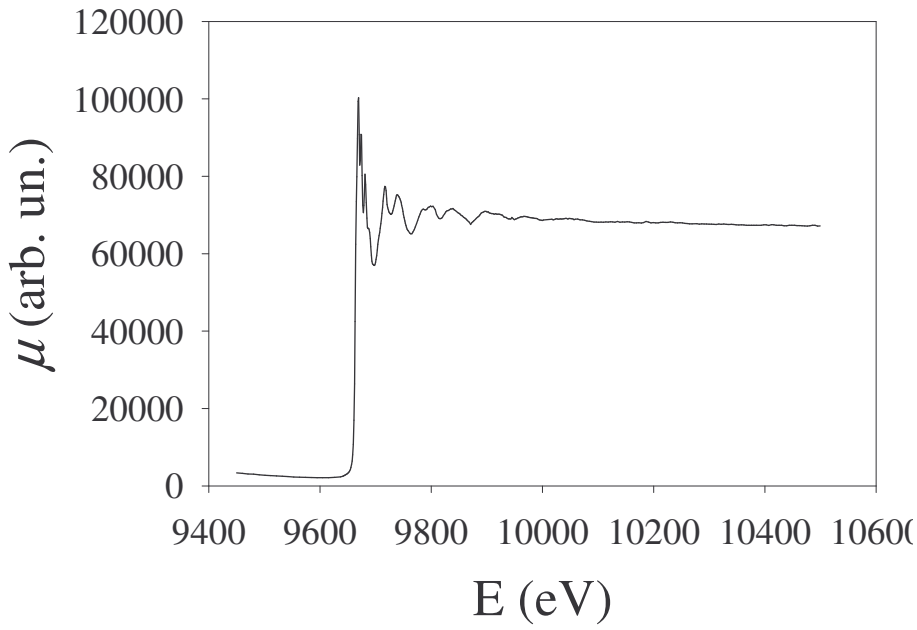

Fig. (4-2): Raw fluorescence data at the Zn-K edge for a ZnO film deposited onto a (1 $\bar{1}$ 0 2) Al_2O_3 single crystal and heated at 600 °C for 20 min (PAR orientation).

The statistical noise was estimated by fitting the spectrum after 10400 eV, *i.e.* where the EXAFS oscillations are no longer visible, with a straight line. After normalization for the edge jump the noise was estimated to be 10^{-3}: this figure is representative of the quality of all the collected spectra. Given that the samples are challenging, this value for the noise should be regarded as very good.

The different reactions of the different films are made apparent by looking at Figs. (4-3) and (4-4). In particular in Fig. (4-3) the Zn–K edge unpolarized XANES spectra are reported. In Fig. (4-4) the Zn-K edge EXAFS spectra (with the relative Fourier Transforms) are reported for the three reacted interfaces before and after the thermal treatments described in the previous chapter. For comparison, in these figures, the spectra of powdered ZnO and $ZnAl_2O_4$ are also shown. In addition, for the sake of better clarity, in these figures the $(0001)_{ZnO} \parallel (11\bar{2}0)_{sapphire}$, $(0001)_{ZnO} \parallel (0001)_{sapphire}$ and $(11\bar{2}0)_{ZnO} \parallel (1\bar{1}02)_{sapphire}$ are labelled A, C and R, respectively, according to the common nomenclature for the sapphire surfaces.

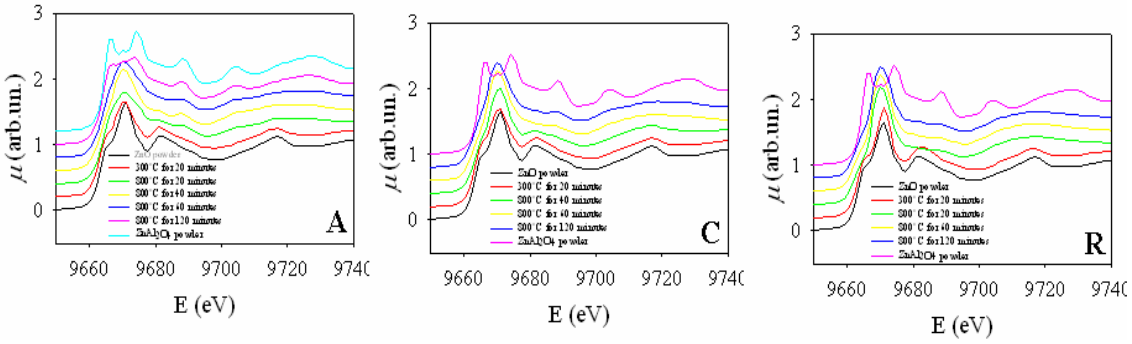

Fig. (4-3): Zn-K edge unpolarized XANES spectra of the three reactive interfaces.

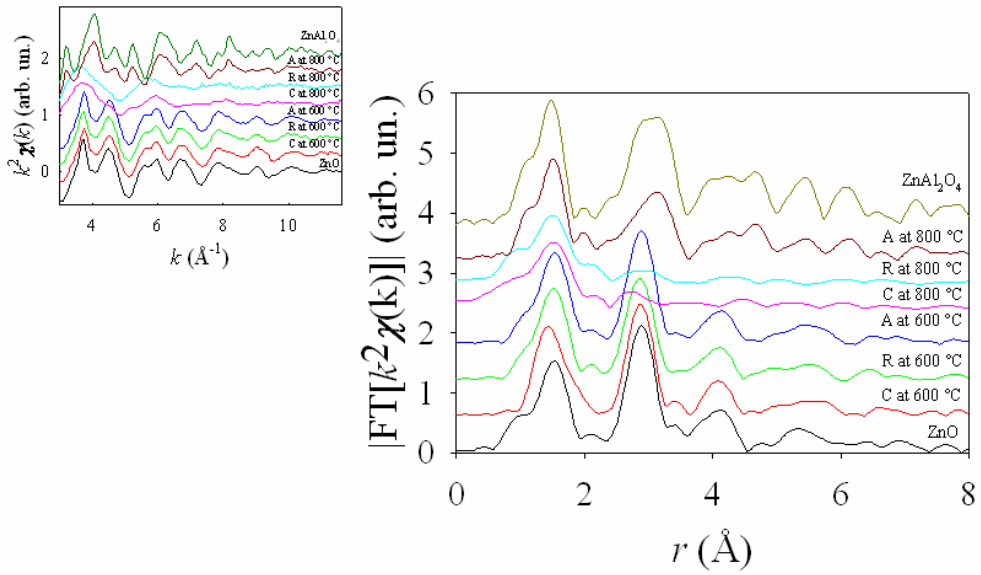

Fig. (4-4): Zn-K edge Fourier Transforms of the three reactive interfaces before and after the thermal treatments. The inset shows the Zn-K edge EXAFS spectra. For comparison purposes the ZnO and $ZnAl_2O_4$ powder spectra are shown.

At 600 °C it is seen at a glance that all the films have the same XANES and EXAFS spectra, and that these spectra correspond very nicely to the one of powdered ZnO. This kind of behaviour is the same till 800 °C when we start to observe some important differences.

When the samples are treated at 800 °C, impressive changes are found in the spectra. In detail, for the film deposited on to the $(11\bar{2}0)_{sapphire}$ single crystal orientation, at 800 °C the Zn–K edge XANES manifold changes from a ZnO-like structure to a $ZnAl_2O_4$-like structure, incrementing the heating time.

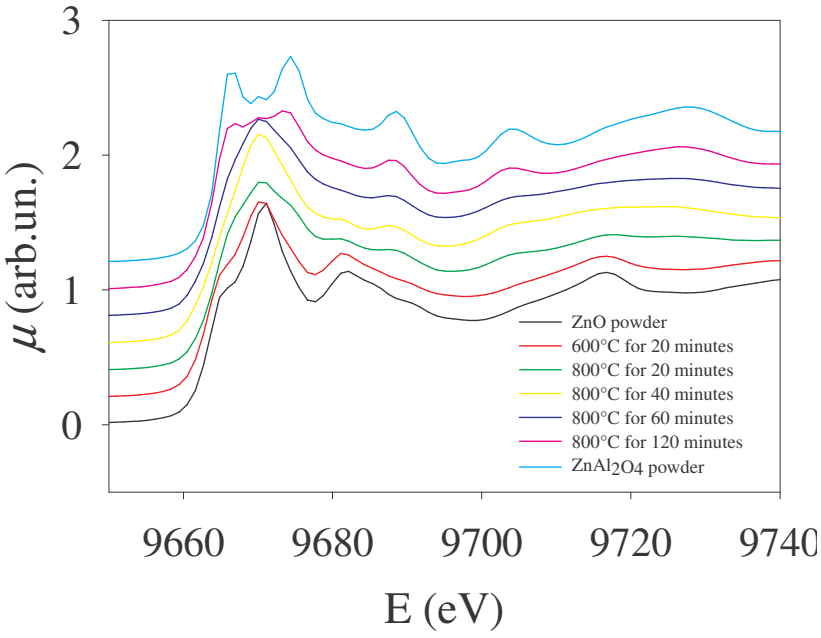

Fig. (4-5): XANES manifold for the reactive interface A changes from increasing heating temperature and time at 800 °C. For comparison purposes the spectra of powder ZnO and ZnAl2O4 are reported.

The XANES spectral features at 9665 and 9683 eV are progressively depressed when compared to those of ZnO, while the principal feature at 9670 eV progressively splits into two peaks passing from ZnO to spinel. In addition, as we can observe, two peaks at 9690 and 9705 eV rise up.

Therefore, for the interface $(0001)_{ZnO} \parallel (11\bar{2}0)_{sapphire}$, the $ZnO+Al_2O_3 \rightarrow ZnAl_2O_4$ reaction takes place at 800 °C and the amount of spinel increases as the heating time increases. The same changes are found if we look at the EXAFS (and to the corresponding FT) spectra in Fig. (4-4) and Fig. (4-6).

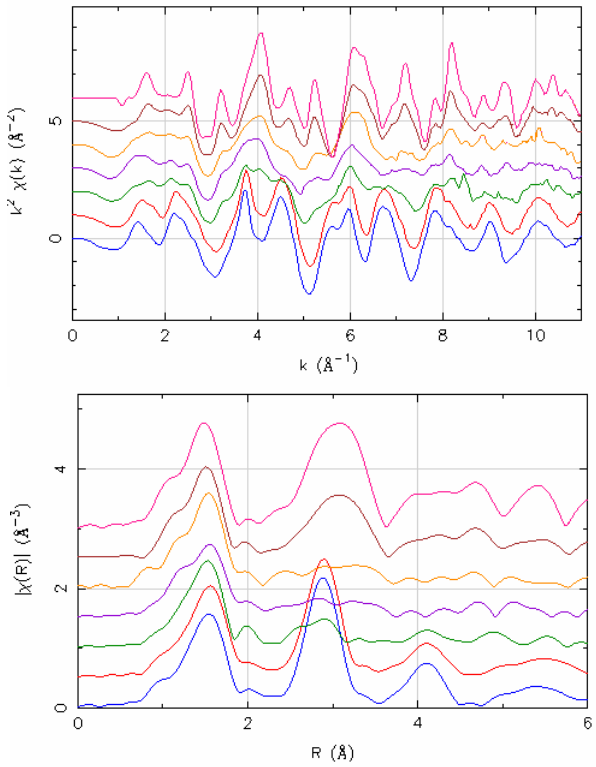

Fig.(4-6): Zn-K edge EXAFS spectra (and relative Fourier Transforms) for the reactive interface A. The different thermal treatments are reported with different colours: red, 600 °C for 20 minutes; green, 800 °C for 20 minutes; violet, 800 °C for 40 minutes; yellow, 800 °C for 60 minutes and brown, 800 °C for 120 minutes. For comparison purposes the spectra of powder ZnO (blu spectrum) and $ZnAl_2O_4$ (pink spectrum) are also reported.

On the contrary, for the $(11\bar{2}0)_{ZnO} \parallel (1\bar{1}02)_{sapphire}$ and $(0001)_{ZnO} \parallel (0001)_{sapphire}$ interfaces, a well different behaviour is found: in particular, in both these cases, the spectral features at 9665 and 9683 eV are progressively depressed when compared to those of ZnO; in addition, these two interfaces show a very similar behaviour, as reported in Fig. (4-3).

The scenario, for these two last interfaces, is here quite intriguing, as demonstrated by the Zn–K edge EXAFS spectra displayed in Fig. (4-4). Inspecting in particular at the first peak of the EXAFS FT, which is due to the nearest neighbours (NN), it is quite apparent that the Zn–O first coordination shell remains almost unchanged, while the peak corresponding to the next nearest neighbours (NNN) becomes strongly depressed after increasing the heating time at 800 °C. Therefore, during the process, the NN coordination of Zn remains tetrahedral as in the ZnO wurtzite-type structure, but with a considerable amount of static disorder in the NNN shell. Additional structural information can be obtained by the EXAFS fitting. The fitting procedure adopted here and carried out by means of the Feff08 code [2] started from the above consideration about the NN and NNN shells and is divided into two procedures, according to the different reaction steps (*i.e.* the different heating time at 800 °C). The fits have been made by using a wurtzite-like structural model, and, to account for the static disorder in the NNN shell, by substituting some of the Zn atoms in this shell with Al, for a total of 12 atoms in the wurtzite structure. This procedure have been carried out for all the spectra of the interfaces $(11\bar{2}0)_{ZnO} \parallel (1\,\bar{1}\,02)_{sapphire}$ and $(0001)_{ZnO} \parallel (0001)_{sapphire}$. For the interface that leads to the spinel, $(0001)_{ZnO} \parallel (11\bar{2}0)_{sapphire}$, the strategy is a little bit different, step by step according to SIMS measurements previously collected, reported in Fig. (4-7).

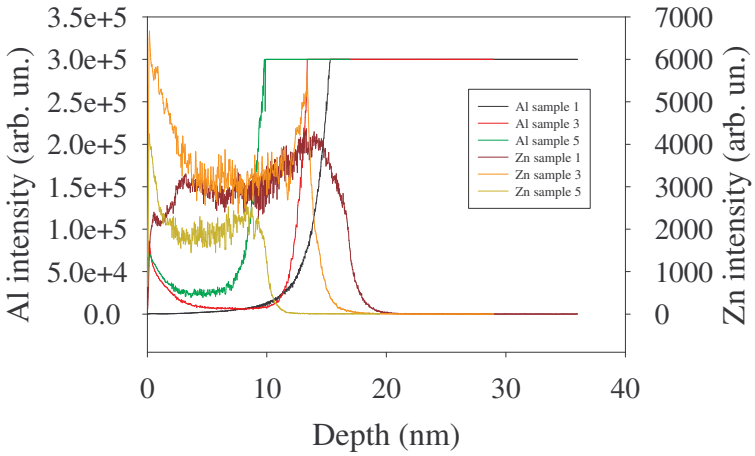

Fig. (4-6): SIMS data collected for the reactive interface $(0001)_{ZnO} \parallel (11\bar{2}0)_{sapphire}$. In this figure the label "sample 1" indicates the interfaces heated at 600 °C, "sample 3" the one heated at 800 °C for 40 minutes and "sample 5" the one heated at 800 °C for 120 minutes.

In Fig. (4-8) the best fit for the interface heated at 800 °C for 120 minutes is shown for interface $(0001)_{ZnO} \parallel (0001)_{sapphire}$ and the results are summarized in Table 3.

(0 0 0 1)$_{ZnO}$ ‖ (0 0 0 1)$_{sapphire}$, model 1				
NN shell				
Atom	***n***	***r***	***σ²/BVS***	***R***
O	1	2.0(1)	0.01(6)/1.76	0.021
O	3	2.0(6)		
NNN shell				
Atom	***n***	***r***	***σ²***	
Zn	12	3.37 (1)	0.03(1)	
Al	0	---		
(0 0 0 1)$_{ZnO}$ ‖ (0 0 0 1)$_{sapphire}$, model 2				
NN shell				
Atom	***n***	***r***	***σ²/BVS***	***R***
O	1	1.89(6)	0.005(6)/1.84	0.011
O	3	2.03(1)		
NNN shell				
Atom	***n***	***r***	***σ²***	
Zn	11	3.11(3)	0.033(8)	
Al	1	3.5(1)		
(0 0 0 1)$_{ZnO}$ ‖ (0 0 0 1)$_{sapphire}$, model 3				
NN shell				
Atom	***n***	***r***	***σ²/BVS***	***R***
O	1	1.88(5)	0.005 (5)/1.86	0.010
O	3	2.03(1)		
NNN shell				
Atom	***n***	***r***	***σ²***	
Zn	10	3.11(3)	0.031(7)	
Al	2	3.16(9)		

$(0\ 0\ 0\ 1)_{ZnO} \parallel (0\ 0\ 0\ 1)_{sapphire}$, model 4				
NN shell				
Atom	***n***	***r***	σ^2***/BVS***	***R***
O	1	1.85(3)	0.005(3)/1.99	0.007
O	3	2.01(1)		
NNN shell				
Atom	***n***	***r***	σ^2	
Zn	9	3.10(2)	0.027(5)	
Al	3	3.15(5)		
$(0\ 0\ 0\ 1)_{ZnO} \parallel (0\ 0\ 0\ 1)_{sapphire}$, model 5				
NN shell				
Atom	***n***	***r***	σ^2***/BVS***	***R***
O	1	1.82(2)	0.004(2)/2.08	0.003
O	3	2.00(9)		
NNN shell				
Atom	***n***	***r***	σ^2	
Zn	8	3.08(1)	0.024(3)	
Al	4	3.13(2)		

Table 3: EXAFS fitting parameters for the spectrum of Fig. (4-7), with different structural models. *r*: distances (Å); *n*: neighbour numbers; σ^2: distance variances (Debye-Waller factors, Å^2); BVS: Bond Valence Sum.

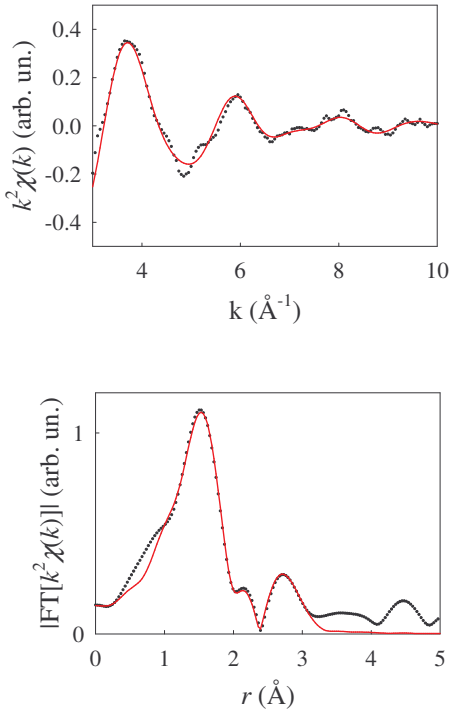

Fig. (4-8): Unpolarised Zn-K edge EXAFS spectra (upper panel) and EXAFS Fourier Transform (lower panel) of the samples investigated in this work. The spectra of powdered ZnO and $ZnAl_2O_4$ are also shown for reference. The experimental data are the dotted line while the red line is the fit.

The best agreement is obtained if one third of the Zn atoms is substituted by Al in the NNN shell of Zn (model 5 of Table 3). In fact, in this last case the GOF (as given by the R-factor that is a parameter that is scaled to the magnitude of the data itself is

defined as $R = \frac{\sum_{i=1}^{N} \left\{ [\mathrm{Re}(f_i)]^2 + [(\mathrm{Im}(f_i)]^2 \right\}}{\sum_{i=1}^{N} \left\{ [\mathrm{Re}(\chi_{data})]^2 + [\mathrm{Im}(\chi_{data})]^2 \right\}}$ and is the sum of squares measurement of the fractional misfit. For good fits to carefully measured data on concentrated samples, R ≥ 0.02.) shows the best figure. An other important parameter is the bond valence sum (BVS) [3], that is a popular method in coordination chemistry to estimate the oxidation state of the atoms. The basic idea is that the valence V of an atom is the sum of the individual bond valences v_i surrounding the atom:

$$V = \sum (v_i) \qquad (4\text{-}14)$$

Here v_i is given by Eq. (4-15):

$$v_i = e^{\left(\frac{R_0 - R_i}{b}\right)} \qquad (4\text{-}15)$$

Where R_i is the length obtained by the fitting procedure, R_0 is tabulated and b is a constant, typically 0.37.

The individual bond valences in turn are calculated from the observed bond lengths.

For Zn the BVS converges to more sensible values by increasing the amount of Al in the NNN shell, up to a Zn/ Al atomic ratio close to 1/3. It should be noted that, even in this case, the disorder is quite important, as indicated by the very high value for the σ^2 parameter. Additionally, it is worth noting that other models have been tested with more Al in the NNN shell: the result is a drastic worsening of the GOF. Somewhat

different results are obtained if the same fitting procedure is applied to the $(11\bar{2}0)_{ZnO} \parallel (1\,\bar{1}\,02)_{sapphire}$ interface (see Table (4) and Fig. (4-9)).

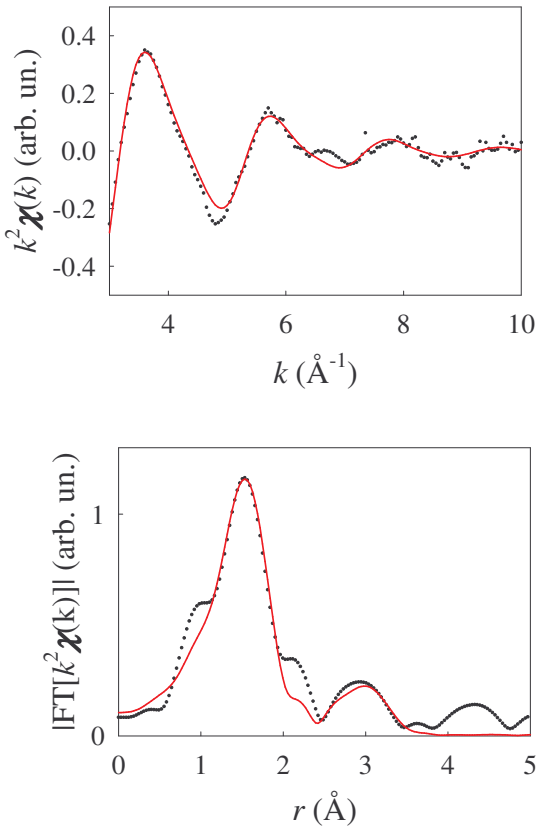

Fig. (4-9): Unpolarised Zn-K edge EXAFS spectra (upper panel) and EXAFS Fourier Transform (lower panel) of the samples investigated in this work. The spectra of powdered ZnO and $ZnAl_2O_4$ are also shown for reference. The experimental data are the dotted line while the red line is the fit.

$(1\,1\,\bar{2}\,0)_{ZnO} \parallel (1\,\bar{1}\,0\,2)_{sapphire}$, model 1				
NN shell				
Atom	***n***	***R***	***σ^2/BVS***	***R***
Zn-O	1	1.99(2)	0.010(4)/1.54	0.030
Zn-O	3	2.079(7)		
NNN shell				
Atom	***n***	***R***	***σ^2***	
Zn-Zn	12	3.68(7)	0.05(4)	
Zn-Al	0	---		
$(1\,1\,\bar{2}\,0)_{ZnO} \parallel (1\,\bar{1}\,0\,2)_{sapphire}$, model 2				
NN shell				
Atom	***n***	***R***	***σ^2/BVS***	***R***
Zn-O	1	2.0(1)	0.01(4)/1.68	0.01
Zn-O	3	2.0(8)		
NNN shell				

Atom	***n***	***R***	σ^2	
Zn-Zn	10	3.23(1)	0.03(1)	
Zn-Al	2	3.22(5)		
$(1\,1\,\bar{2}\,0)_{ZnO} \parallel (1\,\bar{1}\,0\,2)_{sapphire}$, model 3				
NN shell				
Atom	***N***	***R***	σ^2***/BVS***	***R***
Zn-O	1	2.0(6)	0.01(2)/1.67	0.008
Zn-O	3	2.0(1)		
NNN shell				
Atom	***N***	***R***	σ^2	
Zn-Zn	7	3.23(1)	0.028(7)	
Zn-Al	5	3.46(3)		
$(1\,1\,\bar{2}\,0)_{ZnO} \parallel (1\,\bar{1}\,0\,2)_{sapphire}$, model 4				
NNN shell				
Atom	***n***	***R***	σ^2***/BVS***	***R***
Zn-O	1	1.90(4)	0.004(4)/1.80	0.016
Zn-O	3	2.037(8)		
NNN shell				
Atom	***n***	***R***	σ^2	
Zn-Zn	6	3.077(8)	0.011(1)	
Zn-Al	6	3.601(8)		

Table 4: EXAFS fitting parameters for the spectrum of Fig. (4-8), with different structural models. *r*: distances (Å); *n*: neighbour numbers; σ^2: distance variances (Debye-Waller factors, Å^2); BVS: Bond Valence Sum.

In this case, while the introduction of some Al results in a improved GOF, the trend is not monotonous and sensible values for the BVS are obtained only when one half of the Zn atoms in the NNN shell are replaced by Al (model 4).It should be noticed that this model, even as is not the one that gives the most favourable GOF, should be considered as the most consistent, as it gives the most reasonable figures for the BVS and errors in the fitting parameters. It may be worth noticing that the fits displayed in Figs. (4-8) and (4-9) do not account for all the features of the EXAFS spectra. Nevertheless, the main structures are well recovered and there- fore the fit procedure can be trust with a sensible confidence.

The fitting procedure for the reactive interface that leads to spinel has been a little bit different because of the continuous changes that we can find in the spectra. The

spectrum of the sample heated at 800 °C for 120 minutes is clearly very well fitted using a theoretical model based on the Zn-Al spinel structure. The spectra of the samples heated at 800 °C for 60 and 40 minutes have been fitted using a linear combination of the spectra of the two parent oxides while the spectrum of the interface heated at 800 °C for 20 minutes has been fitted using a model similar to those employed for the two interfaces that don't lead to $ZnAl_2O_4$ The fitting strategy is actually divided into two main steps according to the reaction extent: the sample heated at 800 °C for 20 minutes a fitting procedure like the one for the two previous interfaces has been adopted. In the case of the samples heated at 800 °C for 40 and 60 minutes, as said before, a sort of linear combination between the ZnO and the $ZnAl_2O_4$ has been choose. We have to notice that at this moment, because of the completely new approach, the fitting procedure is still in progress and we are not able to give further information on this side of the work.

4.6. - REFERENCES

[1] F. D'Acapito, S. Colonna, S. Pascarelli, G. Antonioli, A. Balerna, A. Bazzini, F. Boscherini, F. Campolungo, G. Chini, G. Dalba, I. Davoli, P. Fornasini, R. Graziola, G. Lichieri, C. Meneghini, F. Rocca, L. Sangiorgio, V. Sciarra, V. Tullio and S. Mobilio,(1998) *ESRF Newsletter* (1998) **30** 042.

[2] A.L. Ankudinov, B. Ravel, J.J. Rehr, and S.D. Conradson (1998) *Phys. Rev. B* **58**, 065.

[3] D. Altermatt and I. D. Brown (1985). *Acta Cryst* **B41**, 244.

5. ID24 AT E.S.R.F. AND THE MICRO-XANES

"If I have seen further than others, it is by standing upon the shoulders of giants."

(I. Newton)

5.1.- WHAT DO WE KNOW ABOUT XANES?

Starting point for treating XANES is the Golden Rule in dipole approximation, Eq. (5-1)

$$W_f = \left(\frac{2\pi}{\hbar}\right)\left|\left\langle \Psi_i \left| \hat{H}_I \right| \Psi_f \right\rangle\right|^2 \rho\left(E_f\right) \qquad (5\text{-}1)$$

Where $\hat{H}_I$ is the interaction Hamiltonian and $\rho\left(E_f\right)$ the density of final states. The Golden Rule allows to reduce a complicated process of dynamical interaction to the calculation of a matrix element between the two initial and final stationary states.

The interpretation of XANES is however by far more complicated [1, 2].

In the proximity of an edge, the X-ray absorption coefficient depends on the transitions of the photo-electron to low-lying un-occupied states. Let us summarize some general properties:

i) The initial stage is a well defined *core level*, almost insensitive to the chemical environment. The edge structures directly reflect the modulations of the density of un-occupied electronic states of lower energy

ii) The initial one-electron core state is localized wavefunction. As a consequence, the edge structures sample the density of final states projected on the absorber site

iii) The initial core state has well defined angular momentum symmetry. By virtue of electric dipole selection rules, the edge structures sample the density of final states projected on the angular momentum.

iv) The excited state corresponding to an X-ray core hole has typically an energy width Γ_h of the order of several eV. The edge structures reflect the density of final states convoluted with the Γ_h width, in addition to instrumental resolution

In crystalline solids, the long-range order simplifies the description and calculation of electronic states. The edge structures are sensitive to the density of un-occupied states in the low-lying part of the conduction band, projected on the absorber site and on angular momentum.

In addition, in the XANES region Multiple Scattering (MS) phenomena become very important. This can be intuitively understood by two considerations: (i) the photo-electron kinetic energy is small with respect to the interaction potential, making more probable the scattering; (ii) the photo-electron mean free path is larger.

According to Eq. (5-2)

$$\chi(k) = \frac{(\mu - \mu_0)}{\Delta\mu_0} \qquad (5\text{-}2)$$

The absorbing coefficient in the EXAFS region can be expressed, in the Single Scatter (SS) approximation, as

$$\mu(k) = \mu_0(k)[1 + \chi_2(k)] \qquad (5\text{-}3)$$

Where μ_0 id the atomic absorption coefficient and χ_2 the EXAFS function.

To take into account MS, Eq. (5-3) is modified as follows:

$$\mu_0 = \mu_0(k)[1 + \chi_2(k) + \chi_3(k) + ... + \chi_n(k) + ...] \qquad (5\text{-}4)$$

In Eq. (5-4), the generic term χ_n represents the contribution due to all possible paths of order n

In principle, Eq. (5-4) contains unlimited number of terms χ_n. Each term χ_n in turn corresponds to different paths, whose number grows very fast when n increases. The relative weight of different terms in eq. (5-4) depends on the photo-electron energy. Going down from hight to low energy, it is useful to distinguish three regimes.

i) in the EXAFS region the terms χ_n of order $n > 2$ are negligible; we are in the SS regime

ii) in the Intermediate Multiple Scatter Region (IMS), only a limited number of terms χ_n ($n > 2$) is important; one can then calculate the absorption coefficient $\mu(k)$ to a good approximation by evaluating only the most significant terms χ_n

iii) at low energies, in the Full Multiple Scatter (FMS) region, the series of eq. (6-4) converges very slowly or does not converge at all; the

absorption coefficient can be obtained only through a direct calculation of the full scattering operator.

MS calculations of XANES ere evidently much more complicated than SS calculations of EXAFS. In particular, it is impossible to interpret XANES by a simple parameterized equation.

If thermal disorder effects are neglected, for each MS path a contribution

$$\chi_n(k) = A(k,\{r\})\sin\left[kR_p + \Phi(k,\{r\})\right] \qquad (5\text{-}5)$$

Should be considered, formally similar to the standard EXAFS formula, but substantially much more complicated. In Eq. (5-5), R_p is half the total photoelectron path. $\{r\}$ is the set of coordinates describing all the interested atoms, A and Φ are functions depending on the potential acting on the photo-electron.

A MS calculation is based on the following steps: (i) assumption of geometrical structure; (ii) sorting of the paths relevant for the application of Eq. (5-4); (iii) calculations of A and Φ function of Eq. (5-5) for each path; (iv) optimization of structural parameters by best fit to the experimental spectrum.

The MS formalism requires the presence of a cluster of atoms surrounding the absorber atom, independently of any degree of long range order.

The complexity of MS calculations is compensated by the possibility of obtaining from XANES three-dimensional structural information.

The scattering paths including only the absorber and one back-scatterer atom contain information only on the two-body correlation function $g_2(r)$. This is the case of EXAFS (χ_2), but also some paths of order $n > 2$

The $g_2(r)$.function is connected to the real distribution $\rho(r)$ by $\rho(r)=4\pi r^2 g_2(r)$.

The scattering paths including the absorber and two different scatterers contain information on the three-body correlation function $g_3(r_1, r_2, \Phi)$, where r_1 and r_2 are inter-atomic distances, Φ the bonding angle

As we can see in this brief introduction to the XANES analysis, the procedure is too complicated and, anyway, to uncertain; for these reasons, in this thesis, we won't perform a detailed XANES analysis (as in the case of EXAFS spectra) but we will use XANES to perform a sort of quantitative study, to follow all the reaction steps and compile a sort of mapping of the reactive interface.

5.2 – EXPERIMENTAL PART

The micro-XANES experiment (CH-2428) was performed at the ID24 beamline at the European Synchrotron Radiation Facility (ESRF), Grenoble that is a nearly unique beamline in its experimental set-up .

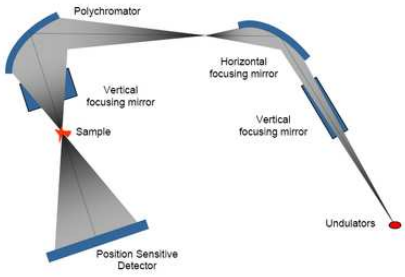

Fig (5-1): Schematic view of the optical layout of the Energy Dispersive X-ray Absorption Spectroscopy beamline ID24 at the ESRF.

The idea aiming such measurement is that, by means of XAS spectroscopy (in particular in the XANES region), is possible to obtain a concentration map of the Zn in the sample. This kind of experiment, unique in its methodology and performed in this case for the first time, has given a lot of evidences about the mechanism and the kinetic of the studied reaction together with important information on the interface structure.

The advantages of an energy dispersive spectrometer as the one at ID24, that features no movement of optics during acquisition leading to an enhanced stability of energy scale, spot size and position combined with micron sized spot and the option of fluorescence detection, have made possible to address 2D mapping with micron resolution on heterogeneous samples, providing full XAS information on each pixel. It is worth nothing that due to the absence of mechanical scanning of the monocromator, the spatial resolution is not affected by the energy scan and remains fixed to the dimensions of the probe. Moreover, the dwell time per pixel is short enough to make it practically possible to acquire 100 x 100 pixel images in a few hours in fluorescence. In this experiment a fluorescence yield version of the conventional (that is based on measurement acquired in transmission mode) dispersive experimental set-up has been exploited. We used the so called "Turbo" XAS demonstrated by S. Pascarelli *et al.* [3-5]. By combing this fluorescence yield variant with the intrinsic speed, stability, and micron scale polychromatic beams achievable on ID24 (as we said before) it's possible to rapidly obtain, by means of simple data analysis, depth and chemical structure profiles (with a resolution of ca. 2 nm) from within the samples prepared as described in chapter 3, that would not otherwise be visible.

As we can observe by looking at Fig. (5-2), to expose the reactive interface that in our case has been the one that leads to the spinel (*i.e.* $(0001)_{ZnO} \parallel (11\bar{2}0)_{sapphire}$), after

heating at 800°C for 20 minutes, the sample was polished as gently as possible with 0.1 μm diamond paste with an angle of about 0.01° with respect to the surface.

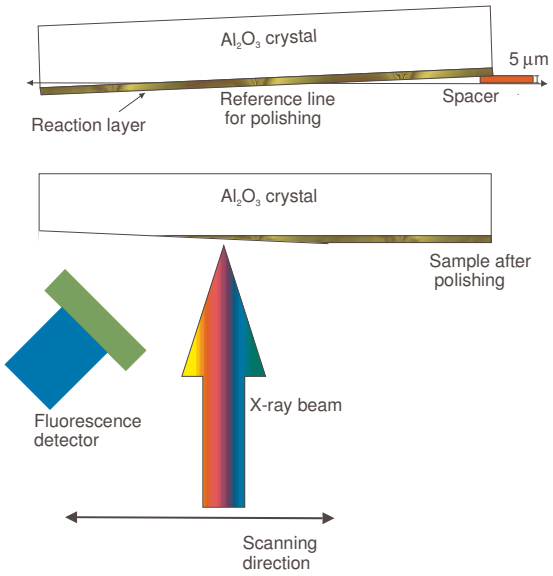

Fig (5-2): Sketch of the experimental method used in this work that schematizes the procedure used for polishing. The lower part is a representation of the arrangement used for the collection of the micro-XANES spectra in fluorescence mode.

With this procedure we have been able to ensure the spreading of the coordinate perpendicular to the surface along those that are parallel. The sample has then been mounted on the ID24 beamline, with the surface perpendicular to the incoming beam. A silicon diode detector, mounted close to the sample at an angle of 45°, was used to collect the XANES spectra in fluorescence mode. The beam was focused with an horizontal FWHM of 7μm and with a vertical one of 150 μm. Zn-K edge spectra have been then acquired across the sample, after calibration in energy by the acquisition of a spectrum of a Zn foil. The horizontal coordinate of the beam corresponds to the scanning direction in Fig. (5-2).

If we look now at Fig. (5-3) it's possible to observe how the fluorescence signal at 9680 eV, that is above the Zn-K edge, changes when the beam is moved along the

scanned direction. It is easy to see how the fluorescence signal increases over a distance of *ca.* 100 μm.

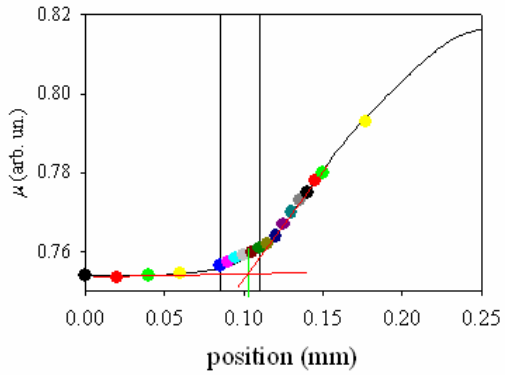

Fig (5-3): Fluorescence signal, excited at 9860 eV, *i. e.* above the Zn- absorption K edge, is plotted vs. the position along the scanning direction (full black line). The interface position (green line) is derived by drawing the double tangents (red full line). The colored dots are refer to the positions where the Z-K edge spectra of Fig. 4 and Fig. 5 have been collected. The black vertical lines are drawn to better put in evidence the interfacial region.

The signal is proportional to the Zn amount in the volume probed by the beam. We remind that the penetration depth of X-rays at this energy is of the order of few μm, and being the ZnO film 20 nm thick, all the Zn in the film has been probed.

The XANES spectra acquired along the horizontal coordinate described before are shown in Fig. (5-4) and (5-5).

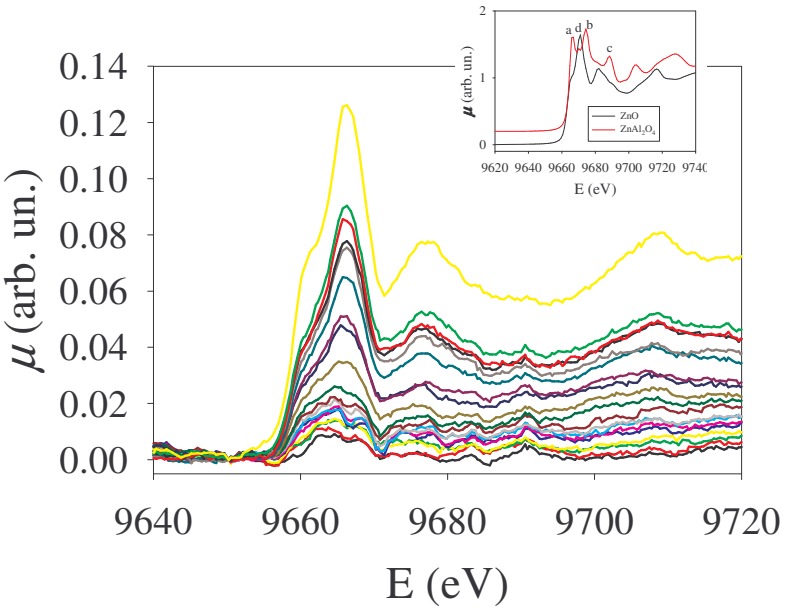

Fig (5-4): Zn-K edge spectra collected along the scanning direction of Fig. (5-2). Different colors refer to the different positions along the gradient, as indicate by the colored dots in Fig. (5-2). In the inset, the spectra of ZnO and $ZnAl_2O_4$ spinel are shown for reference.

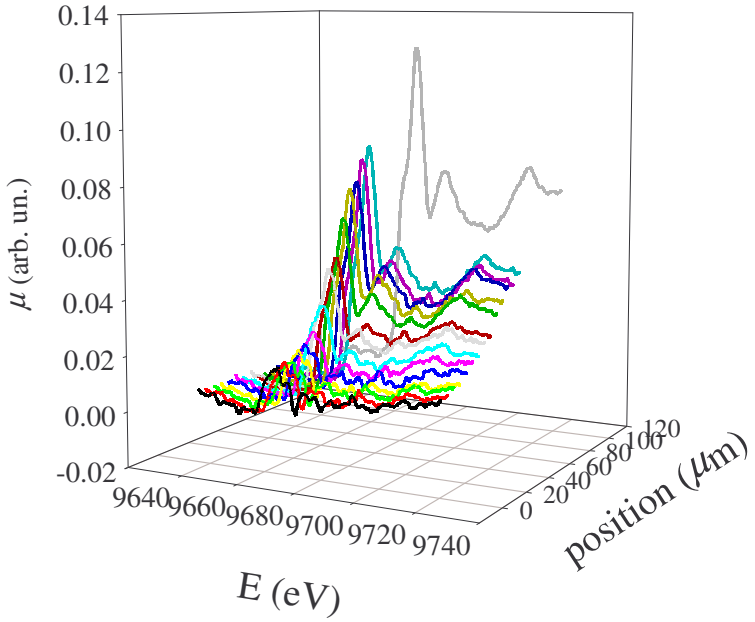

Fig (5-5): 3D visualization of the Zn-K edge XANES spectra reported in Fig. (5-3) anc collected along the direction of Fig. (5-2)

Looking at this figures, it's possible to observe that: (i) the spectral density, and in particular the edge jump, is a direct measure of the Zn amount probed by the beam (as said before) and, for this reason, Fig. (5-4) and (5-5) are equivalent in some way to a

concentration depth profile; (ii) the XANES manifolds change in shape as the beam is moved far from the interface. A comparison with the Zn-K edge XANES spectra of ZnO and $ZnAl_2O_4$ spinel reported in the inset of Fig. (5-4), demonstrates that far from the interface the spectra are almost identical to that of pure ZnO. On the contrary, close to the interface, the edge region is characterised by a more complicated shape. A three peak structure, similar to that of the $ZnAl_2O_4$ spinel may be observed below the interface. In addition, the XANES manifests changes in shape as the beam is scanned across the sample and, in the time line of the growth processes, further away from the interface. These changes can fingerprint phases, and mixtures thereof; they may also contain information regarding the local density of empty states projected onto the photoabsorber, and thereof can reveal deformations of the structure and levels of substoichiometry in the growing oxidic layer.

In order to make these consideration more clear, a sort of map is plotted in Fig. (5-6). and, more in detail, in Fig. (5-7) that represent a zoom of the area that comprends the reactive interface.

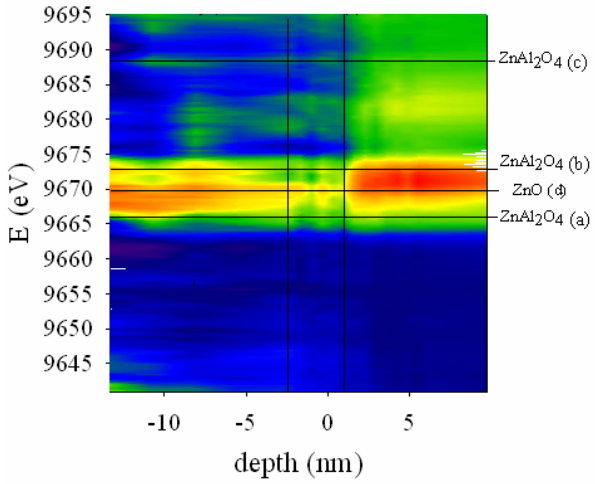

Fig (5-5): Map of the normalized XANES spectra, plotted as a function of the depth along the gradient. The normalization has been made by assuming unit absorption at 9720 eV. Horizontal lines are drawn in correspondence to the mail spectral features of ZnO and $ZnAl_2O_4$, according to the inset of Fig. (5-4). The color intensity scale is shown on the right of the zoom of Fig. (5-6). For better clarity evidencing the interfacial region, are shown.

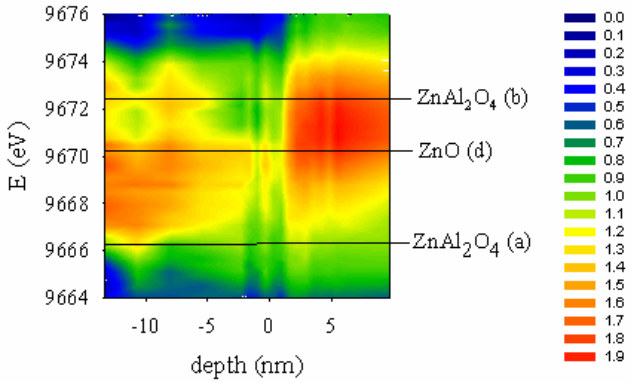

Fig (5-6): An enlarged plot is made in order to better visualize the edge region and the changes in the XANES manifold along the reacting film.

Assuming that the plateau in Fig. (5-3) corresponds to the Al_2O_3 crystal, and that the saturation occurs when the whole ZnO film is in the beam, then the horizontal coordinate of Fig. (5-3) can be easily converted in depth values. In Fig. (5-5) and in Fig. (5-6), therefore, the XANES spectra have been mapped as a function of depth.

In Fig. (5-5) the XANES spectra are normalized and in this way the Zn amount is thought constant. This emphasises the difference in the spectra. Lines are drawn at energies corresponding to the main spectral features of ZnO and $ZnAl_2O_4$. It is clearly seen that, as the depth increases, an abrupt transition from a ZnO-like to a $ZnAl_2O_4$ structure of the spectra is detected. This is a clear demonstration that a chemical reaction is taking place at the interface, and that the experimental method described in this work is capable of probing the interfacial reaction and possibly to give important information on its kinetics and mechanisms. In fact, the relative intensities for peaks (a) and (b) are clearly not correct for the bulk spinel in the early stages of growth. Indeed the most intense feature in the XANES, near the interface, appears in between peak (a) and peak (d) – the most intense feature for the ZnO. There are several causes that can

originate this effect, namely surface relaxation, strain relaxation within the nascent film, other forms of disorder, presence of a transient phase(s) etc.

This experiment was the first of this kind that has ever been performed. For this reason, we started with the interface $(0001)_{ZnO} \parallel (11\bar{2}0)_{sapphire}$ that ensures us the spinel formation (as we observed from fluo-XAS measurements described in chapter 4). The idea was, then, to pass to the other two interfaces but the work to obtain the perfect beamline set-up and all the alignment of the optics takes a lot of time and unfortunately, because of the totally new approach of this kind of study, we could not perform other measurements. However a new proposal has been submitted at the ESRF to continue these kind of measurements on the same surface for different extent of reactions and on the other two reactive interfaces.

5.3 – REFERENCES

[1] D.C. Konigsberger and R. Prins eds, X-ray absorption: principles and applications techniques of EXAFS, SEXAFS and XANES (J. Wiley, New York) 1998.

[2] B. K. Agarwal, X-ray Spectroscopy (Springer, Berlin) 1991.

[3] S. Pascarelli, O. Mathon, M. Munoz, T. Mairs and J. Susini (2006) *Journal of Synchrotron Radiation* **13**, 351.

[4] . Munoz, V. De Andrade, O. Vidal, E. Lewin, S. Pascarelli and J. Susini (2006) *Geochemistry Geophysics Geosystems* **7**, Q11020 .

[5] M. Andreani, O. Grauby, A. Baronnet, and M. Munoz (2008) *European Journal of Mineralogy* **20**, 159.

6. ID03 AT E.S.R.F. AND THE SURFACE DIFFRACTION HELP THE TRADITIONAL XRD

"This isn't right. This isn't even wrong."

(W. Pauli)

6.1 - SURFACE DIFFRACTION: THE YOUNG SISTER OF TRADITIONAL XRD

Surface science is a subject that has grown enormously in the last decade, partly because of the availability of new electron-based tools, such as synchrotrons: satisfactory signal levels are obtained for surface of all but the lightest elements.

On the contrary, as we said in previous chapters, interface science is still in its infancy as far as a structural analysis is concerned.

In this chapter the X-Ray Diffraction and its application to the study of surfaces and interfaces of our models are presented.

Fig. (6-1) introduces the special case of diffraction from a surface. We have to consider two cases: (a) an ideal two-dimensional (2D) monolayer; (b) a truncated 3D crystal. The top layer could have a structure of its own, or it could be a simple continuation of the bulk, with slight modification; (c) interface. Either one or both media may be crystalline and we can apply the traditional diffraction formulae.

As we said in the introduction we can simulate the different situations by means of a model that uses a single crystal on which we deposit the second reactant in form of film that can be very thin (to simulate the quasi-2D situation) or thicker and thicker to arrive at a 3D situation. The film thickness obvious depend on the situation we desired and on the important of the surface interactions we want to study.

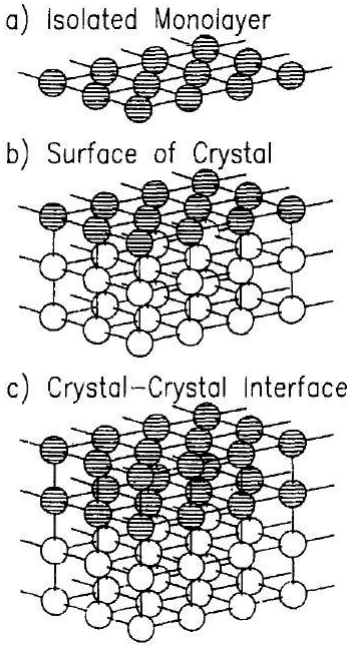

Fig (6-1): Schematic picture illustrating 2D layers existing at surfaces and interfaces. (a) isolated monolayer, (b) surface of crystal, (c) crystal-crystal interface

The diffraction from all the three cases can be described using Eq. (6-1):

$$A_4 = A_0 \frac{e^2}{mc^2} \frac{1}{R_0} F(\bar{q}) S_{N_1}(\bar{q} \cdot \bar{a}_1) S_{N_2}(\bar{q} \cdot \bar{a}_2) S_{N_3}(\bar{q} \cdot \bar{a}_3) \qquad (6\text{-}1)$$

Where A_4 is the amplitude of the wave that comes from a scattering electron, e and m are the electron's charge and mass, R_0 is the distance to the observer, $\bar{q}$ is the vector distance between the ingoing wavevector $\bar{k}_i$ and the outgoing vector $\bar{k}_f$, $F(\bar{q})$

is the sum over all the atoms within one unit cell of the structure factor. For the time being, we will consider the case of large crystal. $S_N(qa)$ is sharply peaked at $q = 2\pi m / a$ where m is an integer, and tends in the limit to a periodic array of δ functions with a spacing of $2\pi/a$.

If we take a_3 to be along the surface normal, the isolated monolayer is handled by setting $N_3 = 1$. The diffraction is then independent of $\bar{q} \cdot \bar{a}_3$, the component of momentum transfer perpendicular to the surface. In 3D reciprocal space, we find the diffraction is a 2D diffraction rods, as shown in Fig. (6-2).

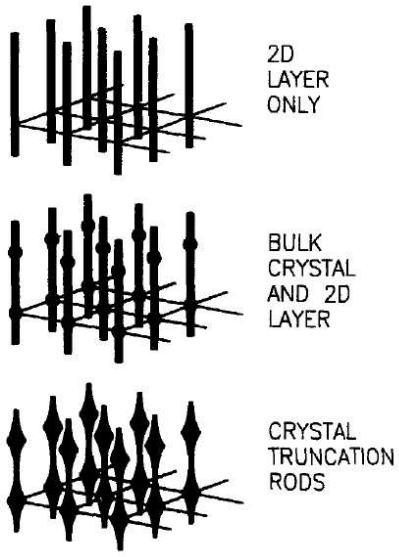

Fig (6-2): Schematic diffraction patterns corresponding to Fig (6-1). (a) for the isolated monolayer, (b) for the surface a 3D crystal, (c) more realistic representation showing variation of intensity along crystal truncation rods (CTRs)

Each rod is a line of scattering which is sharp in both directions parallel to the surface and diffuse in the out-of plane direction. These rods are the chief characteristic of diffraction from the surfaces.

In our experiment, if we were to measure at any point along one of these reciprocal space rods, we would also obtain some intensity, but if we measured in between them we would measure nothing because of the in-plane δ function. The usual form of presentation of such data is in the form of a *scan* or linear slice through space cutting across one of these features. Notice that we always talk about measurements in the reciprocal space.

6.2 – EXPERIMENTAL PART

The surface diffraction beamline at ESRF has been designed to perform diffraction experiments from vertical and horizontal sample surfaces. For this reason two consecutive hutches has been installed. [1]

The sample can be oriented by means of four rotary stages. A horizontally mounted rotary table allows rotation around a vertical axis (μ). A circle (φ) with its rotation axis along the normal of the sample surface is mounted in a double cradle (χ) that allows rotation around an axis in the sample surface. The chi and phi stages are mounted on another rotation stage (θ) with its axis in the horizontal plane along the surface normal. Two translation stages, one vertical and another horizontal along directions perpendicular to the incoming x ray beam, allow to align the center of the diffractometer with the incident beam. The detector has two degrees of freedom δ and γ. The angle δ allows to set the scattering angle in the plane of the sample surface. This is achieved by two synchronized rotary tables with a common axis collinear with the θ axis. The angle γ allows to detect diffracted beams out of the sample surface plane. It may vary from 0° to 47°. It is achieved by a combination of a translational and a rotational stage. Due to this, the distance from the sample to the detector increases with increasing $\boldsymbol{\gamma}$.

All the motions are driven with step motors having rotational encoders in the shafts. The diameter of the confusion sphere of the φ, χ, and θ circles was measured under an axial pulling force of 1000 N and it was found to be 40 μm. The six rotation angles allow a large flexibility in operating conditions since they combine the four-circle [2] and z-axis geometries [3] This results in an enhanced region of access in reciprocal space in the direction perpendicular to the sample surface. In each geometry the angle of incidence or the exit angle of the x rays can be chosen. At the same time the surface normal can be aligned in the horizontal plane if it is desired.

The reactive interface $(0\ 0\ 0\ 1)_{ZnO} \parallel (0\ 0\ 0\ 1)_{sapphire}$ was fired at 800 °C for 120 minutes and a solid state reaction takes place to form an unknown compound with an unknown crystal structure: the morphology of the reacted interface is shown in Fig. (6-3).

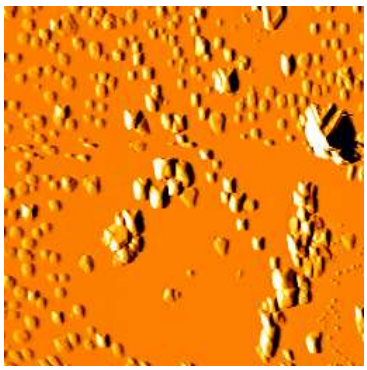

Fig (6-3): AFM image of the interface $(0\ 0\ 0\ 1)_{ZnO} \parallel (0\ 0\ 0\ 1)_{sapphire}$ heated at 800 °C 120 minutes

To obtain further structural information, the sample was mounted on the z-axis diffractometer of ID03 (EH1) (Exp. CH-2814) and surface diffraction patterns have been acquired. We acquired diffraction effects from the nanocrystals on the sapphire surface. An example of an *l* scan for h = 1, k = 1 (black line) and h = 1, k = -1 (red line) (where the Miller indexes are referred to the sapphire unit cell) is reported in Fig. (6-4).

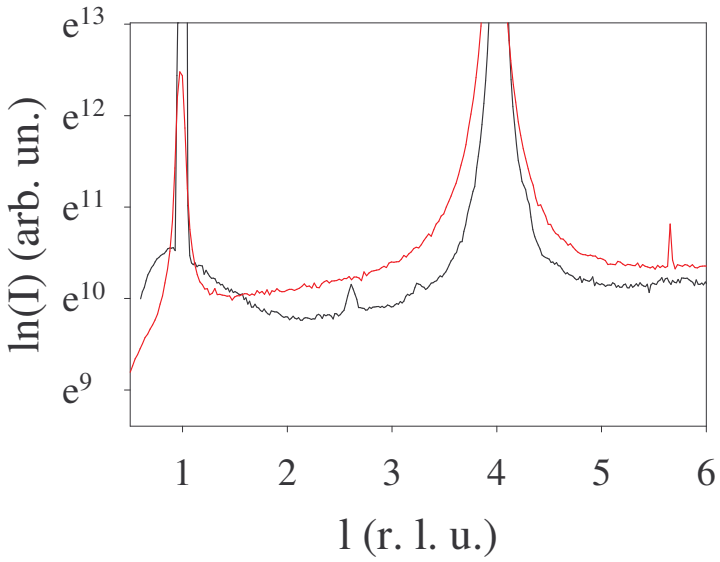

Fig (6-4): Scan for h = 1, k = 1 (black line) and h = 1, k = -1 (red line); in addition to the peaks of Al_2O_3, peaks at non integer l values (2.6, 3.28 and 5.65) are evident

In addition to the peaks of Al_2O_3, peaks at non integer values of *l* (2.6, 3.28 and 5.65) are apparent and are attributed to the nanocrystals formed on the surface during the solid state reaction. In Fig. (6-5) is reported an *h* and *k* scans for *l* = 5.65.

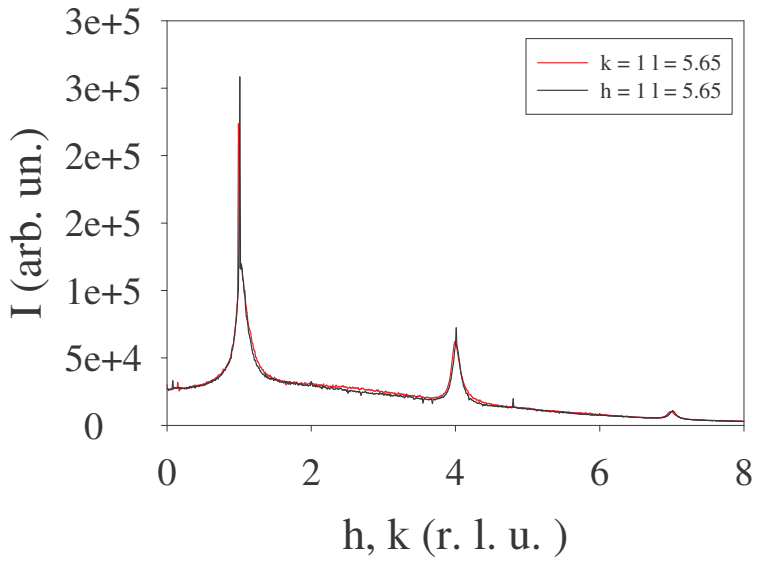

Fig (6-5): h scan (red line) and k scan (black line) for l = 5.65 and k(h) = 1, respectively

After a series of measurements we have been able to collect 25 reflections, as the two described in the examples, that are for sure due to the nanocrystals formed during the reaction. These reflections could be indexed, by means of an *ad hoc* software developed by G. Spinolo, in the hexagonal system with lattice constants a = 4.767(10) Å and c = 27.614(57) Å. It should be noted that the hexagonal symmetry could be due to a topotactic relationship between the sapphire and the nanoscrystals. However, the value of the c lattice constant is quite definite, and it's large value points towards a very complex crystal structure.

Also in this case, the completely new approach of the measurements (that is not a traditional form of Crystal Truncation Rods) and the difficulty in the identification and centering of the nanocrystals on the surface, takes a lot of time for the optimization of the beam-line set-up and focusing and for this reason just one reactive interface at one extent of reaction have been analyzed. We selected one of the interfaces that doesn't leads to the spinel because: (i) we know that the interface $(0001)_{ZnO} \parallel (11\bar{2}0)_{sapphire}$ give a reaction product the $ZnAl_2O_4$; (ii) our priority was to try to understand the structure of at least one of the unknown crystal structure of the products that are not spinel; (iii) the beamline alignment and centering procedures were easier.

Future experiments have been planned to continue such kind of measurements to have further insights about the new compound formed on this surface but also on the other one that doesn't leads to the spinel. Other important information can be obtained by perform such kind on diffraction methods on the interfaces fired at 800 °C for intermediate amount of time, also for the one that leads to the spinel to clarify the mechanism.

6.3 – REFERENCES

[1] S. Ferrer and F. Comin (1994) *Rev. Sci. Instrum.* **66**, 1674.

[2] W. R. Busing and H. A. Levy (1967) *Acta Cryst.* **22**, 457.

[3] J. M. Bloch (1985) *J. Appl. Cryst.* **18,** 33.

7. AFM AND ED : THE WAY TO SEE THE INVISIBLE

"God made solids but surfaces are work of the devil"

(W. Pauli)

7.1 – ATOMIC FORCE MICROSCOPY EXPERIMENTAL PART

AFM images were collected with an Autoprobe CP Research scanning probe microscopy (SPM,VEECO), operating in contact mode, by means of sharpened pyramidal silicon tips (curvature radius < 20 nm) onto V-shaped cantilevers (resonant frequency, 120kHz; force constant, 0.5N/m). For each analysed sample, scans of different areas were carried out with a resolution of 512 pixels and a scan rate ranging between 1.0 and 1.5 Hz. A standard second-order flattening processing of the images was performed in order to correct the scanner non linearity.

Let's start to analyze each reactive interface in detail.

* $(0001)_{ZnO} \parallel (11\bar{2}0)_{sapphire}$

Looking at this reactive interface it is clearly seen that the morphology is quite stable during the reaction forming the Zn-Al spinel.

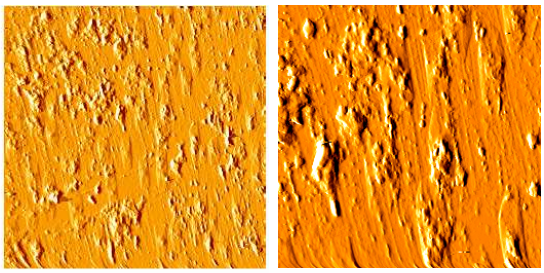

Fig (7-1): AFM images of the reactive interface $(0001)_{ZnO} \parallel (11\bar{2}0)_{sapphire}$ that leads to the spinel heated at 800 °C for 120 minutes. The left photo is a 50 x 50 μm section while the right is a section of 20 x 20 μm. The morphology of the starting interface is reported in Fig. (3-4) of Chapter 3.

A zoom section of 2 x 2 μm took in the smoother area confirm the stability of morphology during the reaction.

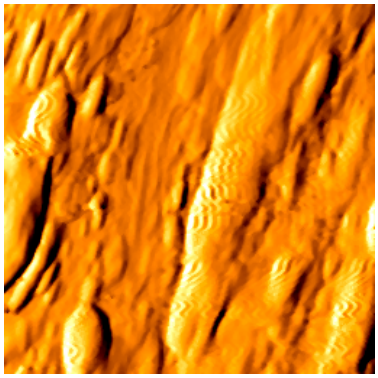

Fig (7-2): AFM photo of the interface $(0001)_{ZnO} \parallel (11\bar{2}0)_{sapphire}$ reported in Fig. (7-1) took in a smooth section of dimension of 2 x 2 μm

The annealed film at 600 °C (as described in Chapter 3) has a mean surface roughness of 7 nm. At the and of the reaction (*i.e.* when we have almost only spinel) the mean surface roughness is of 20 nm.

* $(0001)_{ZnO} \parallel (0001)_{sapphire}$ **and** $(11\bar{2}0)_{ZnO} \parallel (1\bar{1}02)_{sapphire}$

These two reactive interfaces have a completely different behaviour if compared with the previous one but very similar between them.

As we can observe in Fig. (7-3) and Fig. (7-4), in fact, it's clearly seen that the initial morphology progressively collapses into quite large prismatic twins, that have dimension of some micrometers, this is evident if we consider that the analyzed section is a 20 x 20 μm square..

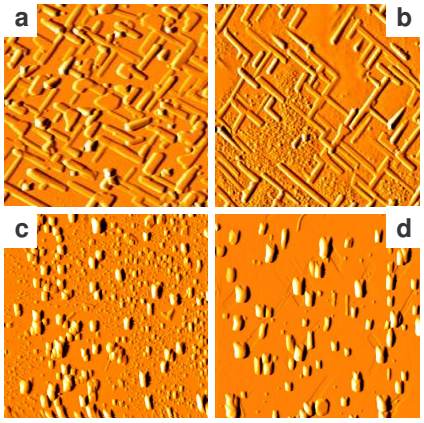

Fig. (7-3): AFM images of the reactive interface $(11\bar{2}0)_{ZnO} \parallel (1\bar{1}02)_{sapphire}$ at increasing heating time at 800 °C: (a) sample heated for 20 minutes; (b) sample heated for 40 minutes; (c) sample heated for 60 minutes and (d) sample heated for 120 minutes

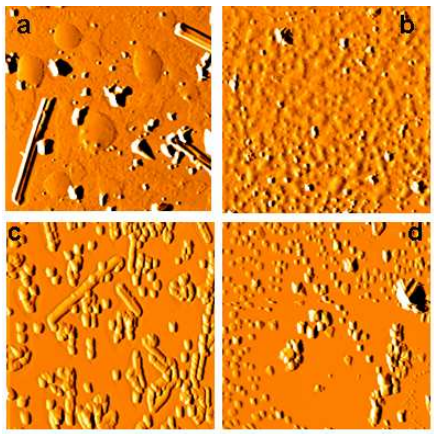

Fig. (7-4): AFM images of the reactive interface $(0001)_{ZnO} \parallel (0001)_{sapphire}$ at increasing heating time at 800 °C:. (a) sample heated for 20 minutes; (b) sample heated for 40 minutes; (c) sample heated for 60 minutes and (d) sample heated for 120 minutes

As we can observe by looking at the two AFM sequences (that are all section of 20 x 20 μm), the reactive interface $(11\bar{2}0)_{ZnO} \parallel (1\bar{1}02)_{sapphire}$ collapses more rapidly than the $(0001)_{ZnO} \parallel (0001)_{sapphire}$. The first is also more regular in its change of morphology, in fact we pass from a regular surface (that is the film heated at 600 °C as shown in Chap. 3) to the formation of small and progressively thin rods, till their decay to form the small crystallites.

For the second reactive interface we can observe a slower change. The surface is in fact quite regular till the heating at 800 °C for 40 minutes and then, suddenly, it decay

to form small rods and crystals. At the end of the reaction what we can observe are only crystals that are smaller then those on the previous interface.

The slower change in morphology of $(0001)_{ZnO} \parallel (0001)_{sapphire}$ respect to $(11\bar{2}0)_{ZnO} \parallel (1\bar{1}02)_{sapphire}$ is very well seen if we look more in detail some section of the samples heated at 800 °C for 20 and 40 minutes for both of them, as reported in Fig. (7-5) and Fig. (7-6):

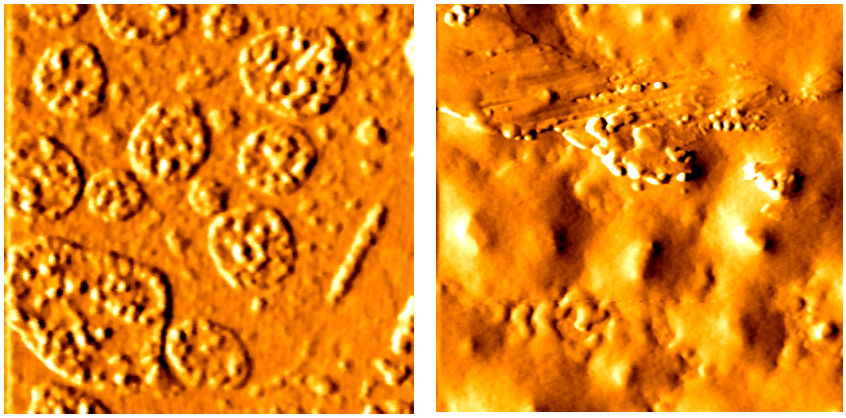

Fig. (7-5): Details of some of the AFM photos of the interface reported in Fig. (7.4). The left image is a section 3 x 3 μm of the sample heated at 800 °C for 20 minutes, while the right one is a section 5 x 5 μm of the sample heated at 800 °C for 40 minutes.

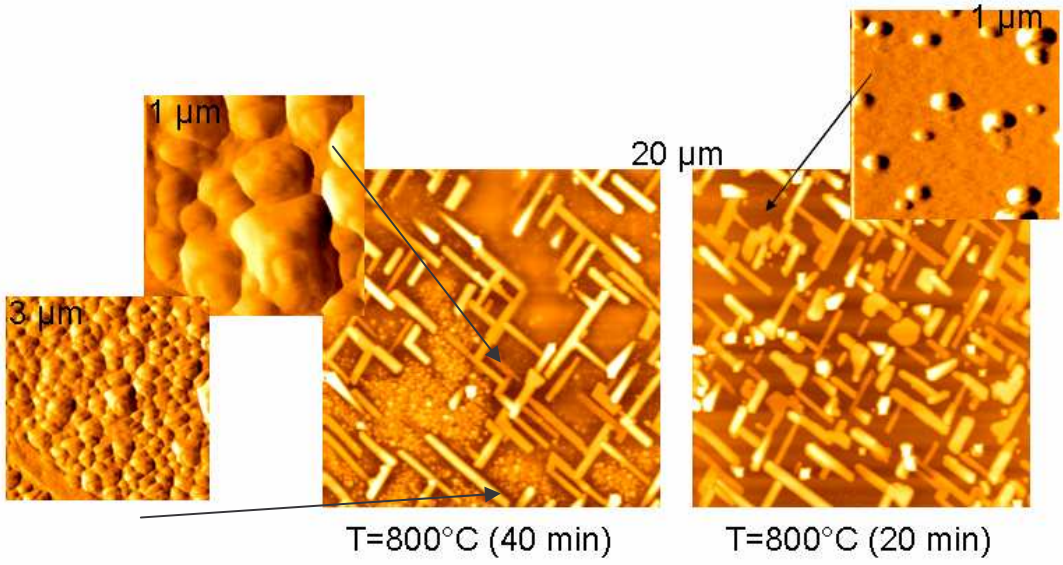

Fig. (7-6): Details of the reactive interface $(11\bar{2}0)_{ZnO} \parallel (1\bar{1}02)_{sapphire}$. The same heating time of the sample of Fig. (7-5) are reported

Also by looking at this AFM photos is clearly seen that the change in morphology of the two interfaces that don't leads to the spinel product is similar but not the same. This fact is confirmed by the different behaviour of the surface even in a very detailed analysis.

This different surface morphology change during the different steps of the reaction, according to the fit results described in Chap. 4, let's us suppose that the products that we have at the end of the reactions for these two orientation are probably two different compounds not yet identified and reported on the phase diagrams.

7.2 – ED MEASUREMENTS EXPERIMENTAL PART

Preliminary electron diffraction (ED) measurements have been performed on a cross section of the crystallites that have been formed on the sample surface of the reactive interface $(11\bar{2}0)_{ZnO} \parallel (1\bar{1}02)_{sapphire}$ and confirmed that this material is highly crystalline, as reported in Fig. (7-7).

The Transmission Electron Microscopy (TEM) measurements were performed on the sample using an FEI Tecnai F20 apparatus operating at 200 kV. The specimens were cooled by a temperature controlled LN holder. Scanning Transimission Electron Microscopy (STEM) images were recorded using a high angle dark field detector.

Unfortunately we were able to collect ED data for only one zone axis, that is 2D information, as showed in Fig. (7-7).

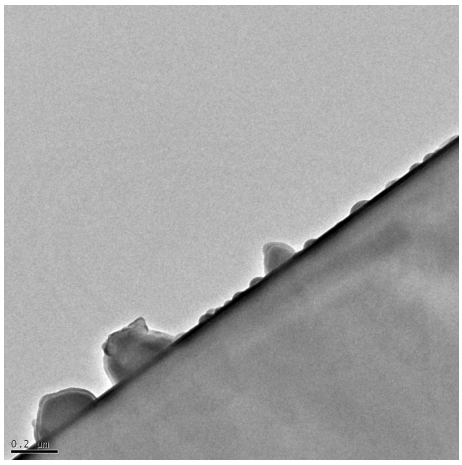

Fig. (7-7): Image of the section of crystallite grown on the reactive interface $(11\bar{2}0)_{ZnO} \parallel (1\bar{1}02)_{sapphire}$ and used for the ED measurements. The small black line in the left side, on the bottom, is the scale and is 0.2 μm.

Observing a diffraction pattern that can be indexed with a centered rectangular lattice having $a \cong 16.0$ Å and $b \cong 4.8$ Å. In lack of 3-D information, no detailed structural characterization could be obtained, but the results are sufficient to infer that a new mixed Zn/Al oxide, not yet reported in the equilibrium phase diagram, is formed. Moreover, the quite large value of one lattice constant is reasonably indicative of a non trivial crystal structure. This confirm, even if on a different (but with similar behavior) reactive interface the formation of completely unknown product(s).

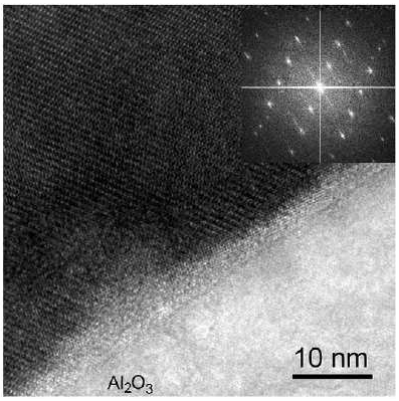

Fig. (7-7): HRTEM image for the $(11\bar{2}0)_{ZnO} \parallel (1\bar{1}02)_{sapphire}$ interface at 800 °C for 120 minutes. The inset shows an electron diffraction pattern of the reaction product

8-TOPOTACTICAL RELATIONS IN $(0001)_{ZnO} \parallel (11\bar{2}0)_{sapphire}$ REACTIVE INTERFACE: A FIRST HYPOTESIS OF MECHANISM

"I want to know God's thoughts; the rest are details."

(A. Einstein)

Given that the samples, the experiments and the completely new approach to the thematic of solid state reactions study in the early stages are challenging, the fact that we have been able to obtain a first idea of mechanism on the interface that leads to the spinel should be regarded as very good point.

For the other two interfaces, obviously, the situation is much more intriguing because of the lack of knowledge about the products that are formed at the end of the reaction. For this reason this chapter will be limited to the study of the reactivity between ZnO and a Al_2O_3 $(11\bar{2}0)$ surface. In this respect this chapter and work should be intended as the first part of a more complete future investigation.

We remind, looking at Fig. (3-3), left part, in Chapter 3 that a huge linear dichroism effect for the Zn-K edge XANES for ZnO film after the deposition is found. As we said in Chapter 3, comparison with literature data at the Zn-K edge for a wurtzite single crystal shows that the ZnO film is highly oriented, with the *c* axis perpendicular to the film surface.

As a first observation we should note that the spectra do not change when the firing temperature is increased up to 600 °C, that is that there are no differences between the sample just after the deposition and after the anneal. On the contrary marked changes are clearly seen when the samples are treated at 800 °C for different amount of time, as reported in Chapter 4, Fig. (4-5) and Fig. (4.6) in which the unpolarised Zn-K edge XANES and EXAFS (with the corresponding Fourier Transforms) are respectively reported and in next paragraph analyzed more in detail.

Fig. (4-5) shows the Zn-K edge unpolarised XANES spectra for the reacted films after increasing heating times at 800 °C. For comparison, in this figure the spectra of powdered ZnO and $ZnAl_2O_4$ are also shown. The unpolarised spectra have been obtained by averaging the spectra taken with the two different polarisations. The average has been done for the sake of comparison with the spectra of the powdered references.

It is observed that for increasing heating time at 800 °C, the Zn-K edge XANES manifold changes from a ZnO-like structure to $ZnAl_2O_4$-like structure when the

$$ZnO + Al_2O_3 \rightarrow ZnAl_2O_4$$

reaction takes place at 800 °C. All the above conclusions are confirmed by looking at the Zn-K edge EXAFS spectra and related FT that are displayed in Fig. (4-6). However, the situation is much more intricate than it looks at a first glance. This can be realised looking at the linear dichroic effects that are shown in Fig. (8-1).

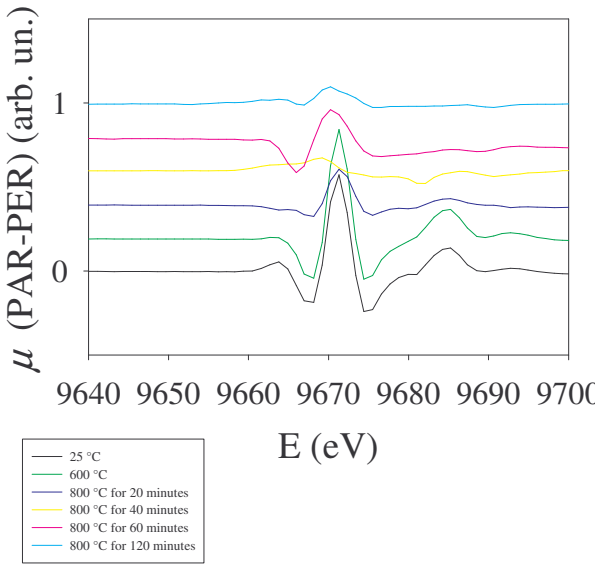

Fig. (8-1): Linear dichroic effect of the analyzed reactive interface.

It can be observed that the effect is strong until 800 °C due to the presence of ZnO only. As a matter of fact when the firing time at 800 °C is increased the dichroic effect initially decreases (spectrum after 20 minutes), then a sudden change in shape is observed after 40 minutes and after 1 hour the dichroic effect is decreased in amplitude but is quite resembling that of ZnO. Increasing now the firing time reduces the intensity of the dichroism.

This complex scenario can be understood in the light of the powder diffraction patterns that are shown in Fig. (8-2).

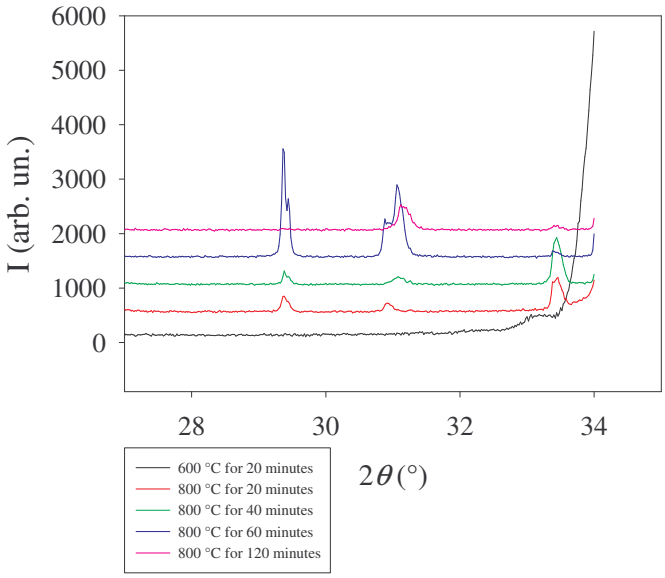

Fig. (8-2): XPRD of the reactive interface showing the change in the ZnO reflections during the increasing heating time at 800 °C

At 600 °C only the ZnO (0 0 2) reflection is seen. This reflection is very large and this is expected as the crystallographic coherence length along this direction can be 15 nm at maximum. In addition a marked decrease in intensity of this reflection can be observed with increasing firing time at 800 °C. Regarding the other peaks that are seen in Fig. (8-2), they are more easily discussed starting from the diffraction pattern of the sample treated at 800 °C for 2 hours. In this case the (2 2 0) reflection of cubic ZnAl2O4 is clearly observable. For the other diffraction patterns this reflection is apparently split into three peaks. These peaks can be indexed as the (1 1 2), (2 0 0) and (1 0 3) reflections of a *tetragonal* spinel structure (space group $I\,4_1/amd$, which is a subgroup of $Fd\bar{3}m$ that is the space group of cubic spinel structure). A remarkable feature of all these reflections is their full width at half maximum (FWHM) which is remarkably small especially if compared to that of the (0 0 2) reflection of ZnO. This is only possible if the [1 1 0] direction of the pseudocubic spinel cell is almost parallel to the film. Our understanding is that these reflections are always outside the scattering

plane and therefore are visible only due to slight misalignment in the scattering geometry. This fact also explains the very small amplitude of these peaks with respect to the (0 0 2) reflection of ZnO, but renders a discussion of the relative intensity nearly impossible. It is reasonably inferred that the first step of the solid state reaction between ZnO and Al_2O_3 is the formation of a *tetragonal* and metastable spinel phase, which gradually transforms into the stable *cubic* $ZnAl_2O_4$ spinel. The presence of the *tetragonal* spinel explains the change in shape of the dichroism. We recall that the *cubic* spinel is optically isotropic and therefore cannot give a dichroic effect. The remnant dichroism which is seen at 800 °C for 1 hour and 2 hours is strongly resembling to that of ZnO and therefore is attributed to the unreacted ZnO film.

We can now discuss the EXAFS data fitting. The data fitting has been done by using a linear combination of the experimental ZnO and $ZnAl_2O_4$ Zn-K edge EXAFS spectra, using as the only fitting parameter the relative amount of spinel translated by the parameter *amp* by FEFF, that in this context assumes the meaning of reaction advancement degree. The reader must be warned that this fitting procedure has been used only for the extent of reaction in which we suppose a sort of tetragonal spinel while for the sample that has been heated at 800 °C for 20 minutes a sort of fitting strategy in which we start from the ZnO wurtzite structure with the substitution of some Zn with Al has been adopted. We have also to remember that in the case of the linear combination fitting procedure, this is not a conventional procedure. The above fitting procedure has been chosen for the aim: (i) of simplicity; (ii) of avoiding the use of unnecessary fitting parameters that unavoidably introduce sources of errors and correlations. In addition the use of the experimental *cubic* spinel spectrum for simulating that of the *tetragonal* spinel is justified by the fact that the local chemical environment of Zn, which is in the tetrahedral site, does not change to a large extent. A

nice confirmation of the above discussion can be obtained by looking at Fig.(4-5) and Fig. (4-6). In Fig. (4-5), the XANES manifold shows a remarkable change in the shape when the heating time is increased from 40 minutes to 1 hour. In Fig. (4-6), at least up to *k* equal to 10 $Å^{-1}$ such a change is not detected. Recalling that the XANES is a probe for the multi-body correlation functions while EXAFS probes just the two-body correlation function we can confirm that the local chemical environment of Zn does not change a lot while the long range structure does when the heating time is increased from 40 minutes to 1 hour.

Observing now in detail the micro-XANES data reported in Chapter 5 is clearly visible how is located the reactive interface between the two parent oxides, that is indicated by the two vertical line in Fig.(5-6) and in Fig.(5.7). Looking at these figures it's seen that there is the diffusion of the Zn into the alumina structure with a strong change in the XANES manifold that becomes completely different both from ZnO and from Al_2O_3.

We can now try to propose a sort of mechanism for the advancement of the reactions in these early stages, that is divided into three principal points:

(i) Diffusion of Zn and O inside the alumina structure

(ii) Rearrangement of the alumina structure and formation of the tetragonal spinel

(iii) Precipitation of the spinel

Another time, looking at the ID24 data we can observe that the formation of the spinel start at a relative long distance from the true reactive interface, this means that the diffusion of Zn and O insight the alumina is a very fast process, and for this reason cannot be the rate determining step.

In the same way the precipitation of the spinel is a very fast step.

All the above considerations let's us suppose, according to the high disorder in proximity to the interface and the completely different XANES and EXAFS spectra from those of the parents oxides, that the driving force of the reaction is the alumina structure rearrangement. In the alumina structure, in fact, that is *hcp* there are a lot of regular thetraedral sites but also a lot of non-regular sites and both can be occupied by Zn arriving from the interface.

The presence of Zn in the alumina structure imposes a structural rearrangement that pass trough a sort of non-stoichiometric spinel that should be a tetragonal spinel. When the quantity of Zn in the alumina structure is enough there is the fast precipitation of the cubic $ZnAl_2O_4$

Obviously, this is a primary hypotesis of mechanism and it has been to be confirmed by other experiments and measurements. We have also to clarify that, taking into account the challenge of the problem, we are not able now to give a sort of same explanation for the other two interfaces, not only because the mechanism seems to be different but also because we don't know till now the structure and the stoichiometry of the products.

CONCLUSIONS

"A scientist in his laboratory is not a mere technician: he is also a child confronting natural phenomena that impress him as though they were fairy tales."

(M. Curie)

In conclusion, in the present work of thesis the reactivity of thin layers (*ca.* 20 nm thick) of ZnO deposited onto differently oriented Al_2O_3 single crystals and the development of a completely new approach, model and procedure (that comprehends different techniques, most of them based on synchrotron radiation) to study the early stages of solid state reactions is reported.

This completely new approach has been selected because the application of the traditional procedure, as indicated by Schmalzried *et al.* (see Introduction and Chapter 1) is in the case of the early stages of the reactions in the solid state, totally un-useful. In fact, we have to remember that for the late stages, the local chemical equilibrium at the interface is attained and long range diffusion is the driving force of the reaction. In the first stages, otherwise, the local chemical equilibrium is not yet attained and, for this reason, the long range diffusion is not the driving force. This field of the study of reactions in the solid state is almost unknown because of the lack of an experimental probe and of knowledge about these stages in solid state reactions.

We built up a model using one of the reactant in form of very thin film (that is 10 ÷ 20 nm) and using a local probe for one of the constituents, for this purpose a completely new application of XAS has been proposed, as reported in Chapter 4 and especially in Chapter 5.

We found that different chemical processes take place at different amount of heating time at 800 °C depending on the topotactic relationships between the ZnO film and the Al_2O_3 single crystals: In particular:

1) Thermal heating at 800 °C causes a spectacular change in the morphology of the $(1\ 1\ \bar{2}\ 0)_{ZnO} \parallel (1\ \bar{1}\ 0\ 2)_{sapphire}$ and $(0\ 0\ 0\ 1)_{ZnO} \parallel (0\ 0\ 0\ 1)_{sapphire}$ deposited layer, with the formation of prismatic twins. In addition, it has been observed that the first interface react faster then the second one.

2) This change in morphology is caused by a chemical reaction between ZnO and Al_2O_3 to form a Zn/Al mixed oxide, or, possibly two different Zn/Al mixed oxides as confirmed by fluo-XAS, EDS and AFM measurements.

3) This(these) compound(s) has(have) not yet been reported in the literature. The Zn-O coordination is tetrahedral and strongly resembles that of the wurtzite structure of ZnO. However, some Al is in the NNN shell of Zn.

4) On the contrary, the $(0\ 0\ 0\ 1)_{ZnO} \parallel (1\ 1\ \bar{2}\ 0)_{sapphire}$ interface yields the $ZnAl_2O_4$ spinel and the film remain more stable in its morphology (as we reported in detail in Chapter 8).

5) The experimental findings demonstrate that an *ad hoc* combination of different techniques with a completely new approach, most of them based on synchrotron radiation, can be a useful tool for investigating the early stages of solid state reactions.

6) It can also be concluded that in the early stages a solid state reaction is controlled by the topotactic relationships between the two reacting solids not only for what concerns the kinetics and mechanism, but even the chemical nature of the product, ad demonstrated by the different final products on the three different alumina single crystal orientation.

Up to now, a sort of first mechanism for the reactive interface $(0001)_{ZnO} \parallel (11\bar{2}0)_{sapphire}$ that leads to the spinel formation may be supposed.

Looking at the combination of the data obtained from the experiments reported in Chapters 4 and 5, together with some previous SIMS results, we are able to suppose that there are for this orientation three crucial steps, that are:

1 – The diffusion of Zn and O into the Al_2O_3 structure

2 – A sort of rearrangement of the alumina structure

3 – The precipitation of the spinel

Taking into account all the experimental evidences obtained in this study we may suppose that, for this kind of reactive interface, the driving force of the reaction is the rearrangement of the alumina structure when the Zn diffuses inside (as reported more in detail in Chapter 8).

Further work is planned to clarify the crystal structure of the new compound(s), and to elucidate the range of solubility of Al in this(these) structure(s), with the aim of gaining further light into the mechanisms and kinetics of these processes for the two orientation that don't lead to the spinel and to better understand the mechanism that, till now, we have only supposed for the interface that leads to $ZnAl_2O_4$.

Other future prospective are the implementation of the described procedure for the study of the reaction between alumina and different metal oxide MO (where M = Mn, Ni, Fe, for example) and of layers of different thickness, to pass from a quasi 2D

situation to a 3D and to better clarify the role of the interface, of the topotactical relationships and to better understand the reaction mechanism in these early stages.

APPENDIX A – THE FEFF CODE

The aim of an EXAFS analysis is to determine the local structural parameters by minimizing the difference between an observed EXAFS spectrum and the theoretical EXAFS calculated from a model of the absorbing site.

The analysis is based on three steps: background (i. e. atomic absorption cross section) subtraction, ab-initio simulation of theoretical signals on the basis on a well defined starting model and multi-parameter fitting.

Many Software packages are available for this analysis (UWXAFS, EXCURVE, GNXAS, etc..).

In our work the UWXAFS package has been used. EXAFS oscillations were extracted from the raw data using the AUTOBK program as implemented in the ATHENA package, using a linear function for the pre-edge region and a cubic spline to mimic the atomic background.

Theoretical amplitude and phase shift functions were calculated using the ab-initio code FEFF 8. The data were analyzed using the FEFFIT program as implemented in ARTEMIS package (version 0.8.006) using as minimization algorithm a modified Levenberg-Marquardt method [1].

Fits were performed directly in k-space to avoid truncation and loss of information due to Fourier filtering.

Fourier filtering was used mainly to check the correctness of the background subtraction and to inspect the data in a qualitative way.

One of the crucial features in obtaining accurate three-dimensional structures is to minimize the number of variables with respect to the number of independent data points. This is achieved by placing constraints and restraints on parameters that are fitted in the calculations.

The analysis of EXAFS can yield the number and types of backscattering atoms, accurate absorber-backscatterer distances and disorder parameters (Debye-Waller factors). When multiple scattering effects are important, also some angular parameters can be obtained.

Background subtraction

Background subtraction is carried out through three steps: a pre-edge background removal using a linear function; a normalization to the edge jump; a post-edge background removal. The last procedure consists in subtracting from $\mu(E)$ a smoothly varying background function $\mu_0(E)$, which approximates the absorption from the isolated embedded atom. The function used to approximate the post-edge background is a third-order polynomial spline whose knots are equally spaced in k space, the flexibility of the spline being determined by the number of knots. The spline and its first two derivatives have to be continuous at the knots and one degree of freedom is associated to each knot; the background function is not required to go through the experimental curve at the knots. The basic idea of the program is that no signal in the Fourier transform of the EXAFS function can have a physical meaning

below a quite small threshold value of R, so that the free coefficients of the spline are chosen in order to minimize the R components below a fixed R value, named R_{bkg}. This means that the method chooses the spline to best fit only the low-frequency components of μ(E). The value of R_{bkg} can be chosen by the user, a good choice being about half the distance of the first shell peak, and determines the maximum number of knots i.e. the stiffness of the spline. From information theory the number of independent points for a sinusoidal function is:

$$N_{ind} = \frac{2\Delta R \Delta k}{\pi} + 2$$

where *R* and *k* are the *k* and *R* ranges of the analyzed data. If the fit is performed from R = 0 to R = R_{bkg}, as in the case of the background removal, the number of independent points is thus:

$$N_{ind} = \frac{2R_{bkg}\Delta k}{\pi} + 2$$

Since each knot is associated with one degree of freedom, the maximum number of knots is the integer part of N_{bkg}^{ind} in the previous equation; the program uses a number of knots equal to $N_{bkg}^{ind} - 1$. The extracted EXAFS function is usually multiplied by a factor k^n to compensate for the rapid attenuation of the EXAFS with increasing *k*. The arbitrary exponent *n* is called the *k*-weighting.

Fourier filtering

The Fourier transform of a *k*-weighted EXAFS spectrum is a complex functionof the distance thus it is related to a radial distribution function. However, because of the presence of a phase factor, depending from both the central and the backscattering atoms, the Fourier transform does not peak exactly at the distances of the backscattering atoms. A ’phase’ correction relating the peak positions to the true interatomic distances

is required. This correction depends on the wave number. The Fourier transform acts as a frequency filtering of the original EXAFS by applying a window function prior to the forward or inverse Fourier transformation. It is thus possible to eliminate noise or unwanted contributions of the EXAFS. However, the use of filtering may distort the EXAFS contribution of one or more scatterers.

Simulations of theoretical signals using FEFF08

In order to analyze the extracted EXAFS function we need to build a starting model, on the basis on which a ab-initio simulation of the absorption cross section is performed. FEFF 8 code implements a Green function approach. A Dirac-Fock atomic code is used to obtain free electronic densities, which are successively overlapped following the Mattheiss prescription in order to obtain a total electron density and to construct Coulomb potential. Then the exchange-correlation potential is added. In FEFF8 there are five different options. By default the program uses a ground-state Von Barth-Hedin potential and the Hedin-Lundqvist (HL) energy-dependent self-energy correction. The total potential is approximated with a Muffin Tin (MT) one, which is flat in the interstitial region and otherwise it is equal to the sum of overlapping, spherically symmetric potentials:

$$V_{tot}(\vec{r}) = V_{mt} + \sum_i V_i \ (\left|\vec{r} - \vec{R}_i\right|)$$

The MT radii, determined using the Normann prescription, are kept fixed. The Dirac equation in the spinor relativistic approximation is then solved to obtain radial wave functions and partial wave shifts, that are necessary to construct the single particle Green function. Finally, the Green function is calculated in the multiple scattering approach: paths with negligible amplitude are rejected and amplitude and phases for all paths inside a definite cluster (the radius of which can be chosen by the user) and

formed by a number of legs ≤ n where n can be chosen by the user, are recorded in different files as a function of the energy. It is possible to insert self consistent corrections in the calculation. This is achieved adding the Self Consistent Field (SCF) card in the input file. If this card is inserted, the program implements an iterative procedure of the calculations of the potentials. In the initial iteration the radii are fixed according to the Norman criterium. On the basis on these radii a charge density and the corresponding Fermi energy are calculated. Then the local Fermi level at each site by requiring no charge transfer is computed and a new density, including charge transfer is achieved. Self consistency is reached when the two Fermi levels and the two densities are equal.

Multi-parameter fitting

The aim of the fitting procedure is to optimize the match between the calculated and the observed EXAFS (χ_{calc} and χ_{obs} respectively) by varying the free parameters. This is done by minimizing the difference between the two EXAFS functions multiplied by the weight k^n,

$$\sum_1^n \left[k^n \left(\chi_{obs}(k) - \chi_{calc}(k)\right)\right]^2 dk$$

Where the sum is over the experimental points N. In FEFFIT the minimization is performed using a modified Levenberg-Marquardt method. The variables commonly used are: a variation in the energy origin (ΔE_0), a number of distance variations to account for structural modification of the starting model, and some DW factors, properly grouped in shells, to account for the effect of thermal motion of the atoms and/or structural disorder. In some cases can be extremely convenient to fix a priori the DW factors to avoid local minima. When multiple scattering effects are important, also angular variables can be inserted the amplitude reduction factor can be either free or fixed to a reasonable value (for example, calculated from FEFF8 from atomic overlap

integrals).

The size of the *k* interval in which the fit is performed is important and it is normally chosen to be as large as the data reasonably allows. The upper limit is chosen on the basis of noise (or hypothetical distorsions) in the XAFS whereas the lower limit is chosen in order to eliminate the region in which the EXAFS series is not convergent. It has been demonstrated that the convergence of the path summation gives the same result as the matrix-inversion method with terms higher than about fifth order only being required near a strong low-energy resonance. Thus, in principle, we should be able to reproduce the entire spectrum by using all the contributions until the fifth order.

Another parameter to be taken into account is the number of legs that are included into the fit of the data. For most systems some paths involving up to five legs make significant contributions (say 20 % of the importance of the most important scattering paths) thus the cut-off of five-leg paths is normally the compromise made in order to minimize the calculation time while still having a very good fit to the experimental data. While the inclusion of multiple scattering paths often does not affect the accuracy of the determination of the bond lengths compared to single scattering analysis, it is essential in order to provide meaningful information on the nature of the donor groups.

Constrained and restrained refinement

A crucial factor in the fitting procedure is to ensure that there are more independent data points than there are variables. Thus it is extremely important to minimize the number of variables. The minimization is achieved by using constraints

and restraints on structural and dynamical parameters.

Constraints are not allowed to vary during the fitting procedure, whereas restraints are placed on parameters such that a bond length or angle is allowed to vary only within a reasonable value that is based on structural information from other sources. In the present thesis only constrained refinement has been applied. It is obvious that this procedure is extremely successful when the system is highly symmetric and constraints are used to make equivalent or very similar bond lengths and bond angles identical. In principle, also the Debye- Waller factors can be calculated and included in the fitting procedure as constraints in order to reduce the number of variables further. Actually this is quite complicated since both static and dynamic disorder are described by the same damping factor. The static disorder is in general unknown and cannot be calculated.

Determinacy

The determinacy of the system is defined as *Ni/p*, where *p* is the number of the fitted parameters and *Ni* is the estimated number of independent data points collected in the XAFS data set. Determinacy in MS analysis of XAFS has a different meaning to the ratio of observations versus variables in X-ray crystallographic refinements. In fact XAFS analysis, at variance with XRD, relies on robust starting models, incorporating information form a variety of sources.

Statistical significance

Three numbers can be used to evaluate the goodness of a fit: χ^2, reduced χ^2 (which we will indicate with χ_v^2) and the R factor. χ^2 and χ_v^2 are defined respectively

as:

$$\chi^2 = \frac{N_{ind}}{N} \sum_{i=1,N} \left[\frac{f_i^{\exp}(k) - f_i^{theor}(k)}{k^n \sigma_i} \right]^2 \quad \text{and} \quad \chi_v^2 = \frac{1}{v} \chi^2$$

where $f_i^{\exp}$ and f_i^{theor} are the experimental and simulated EXAFS functions multiplied by the factor k^n and n is the k –weighting; σ_i is the uncertainty at point E_i; N_{ind} is the number of independent points; v is the number of the degrees of freedom of the system, defined as $N_{ind} - p$ (p being the number of the free parameters). The pre-factor N_{ind}/N in the expression of χ^2 is introduced in order to remove the arbitrariness of the calculation of the number of evaluations N in which the sum is performed. The R factor is defined as said in Chapter 4.

This goodness of fit index is currently used, since the estimation of the uncertainty σ^2 in EXAFS data is notoriously problematic, making the use of chi-square statistic usually meaningless. In fact, by assuming that the uncertainty is all due to random noise, χ_v^2 values much larger than 1 are usually obtained, also in the presence of good fits (*i. e*. at relatively low values of the R factor). This situation is attributed to inadequacies of the model and/or to systematic experimental errors.

However, the R factor is not a proper statistical measure, as it doesn't incorporate any measure of data quality. This makes the comparison between two fits in terms of R factor extremely delicate, since we cannot associate a standard deviation to this goodness of fit index. Usually to compare two fits the chi-square statistics is thus used.

References

[1] J.J. Mor (1977) *Lecture notes in mathematics*, Springer.

PUBBLICATIONS – SONIA PIN

P. Ghigna, S. Pin, G. Spinolo, M. A. Newton, M. Zema, S. C. Tarantino, G. Capitani and F. Tatti "Pushing microbeam techniques to the nanoscale to get structure and composition of buried interfaces" *Science* submitted

P. Ghigna, S. Pin, A. Speghini, M. Bettinelli and T. Tsuboi "Unusual Ln^{3+} substitutional defects: the local chimica environment of Er^{3+} and Eu^{3+} in nanocrystalline Nb_2O_5 by Ln-K edge EXAFS" *Journal of Solid State Chemistry* submitted

S. Pin, P. Ghigna, G. Spinolo, E. Quartarone, P. Mustarelli, F. D'Acapito, G. Calestrani e A. Migliori "Nanoscale formation of new solid-state compounds by topochemical effects: the interfacial reaction of ZnO with Al_2O_3 as a model system" *Journal of Solid State Chemistry*, **182** (2009) 12911296

G. Prando, P. Carretta, S.R. Gibilin, J. Lago, S. Pin e P. Ghigna "Diluition effects in $Ho_{2-x}Y_x$ Sn_2O_7: from the spin ice to the single ion magnet" *Journal of Physics: conference series* **145** (2009) 012033

AKNOWLEDGEMENTS

Thunder is good, thunder is impressive, wrote Mark Twain, *But it is the lightning that does the work*. Often it's some people's thunder, which holds the credit and the attention; but is also other's people lightning one of the main factors in group success. And, indeed, the research presented was possible thanks to a lot of people I shared time and work with.

Prof. Paolo GHIGNA welcomed me with him for my PhD. His informal way of communicating opinions and discussing things has been a warm companion of my daily life. No need to be "dressed up" made me enjoy every minutes, and the autonomy I had helped me in relieving the stress that sometimes comes with research. His direction has been invaluable to pursue everyday and longterm results.

Prof. Michel DUCLOT and Dr. Francesco D'ACAPITO gave me the opportunity to spend one of the most fruitful, interesting and greatest periods in Grenoble. Two great group leader and scientists, they made me feel at home and relaxed every day of my stay. Their great advices and their being keen on listening to people and guiding them towards their goals are incredibly valuable qualities.

Marco MOLINARI, PhD Student and classmate, indefatigable scientist; his nights out had an incredible effect as he was every morning full of energy (of course, after some coffees)

Dr. Filippo MAGLIA and Dr. Marco SCAVINI, two of the funniest people I met.

Prof. Giorgio SPINOLO that taught me the precision and order in daily research.

Alice GARBERI and her potassium manganate gave me the opportunity to learn the pain and satisfaction to be a supervisor; probably the pain was more on her side and the satisfaction on mine.

I enjoyed working next to Dr. Michele ZEMA and Dr. Serena TARANTINO that worked on the same project.

Others members of the group also need to be mentioned; Prof. Umberto ANSELMI TAMBURINI and Primo BALDINI, Ilenia TREDICI, PhD, and Beatrice MARONI, PhD Student. Their help, nice talks and opinions have been friendly accompanying.

I would also like to remember all the GILDA beamline and LEPMI staff. Everyone there was contributing to make my stay great and, therefore, I would like to mention Dr. Lorenzo MALAVASI.

RINGRAZIAMENTI

Thunder is good, thunder is impressive, scriveva Mark Twain, *But it is the lightning that does the work*. Molto spesso sono le persone come il tuono che ottengono crediti e attenzioni, ma ci sono anche le persone "luce" che rappresentano i protagonisti principali del successo di un lavoro di un gruppo. A questo proposito, la ricerca presentata qui è stata possibile grazie a tante persone con cui ho condiviso tempo e lavoro.

Ringrazio il Prof. Paolo GHIGNA che mi ha accolta per il mio dottorato. Il suo modo informale di comunicarmi la sua opinione e di discutere è stata una piacevole componente della mia vita quotidiana. La necessità di non essere sempre "sull'attenti" mi ha permesso di divertirmi ogni minuto e l'autonomia che mi ha lasciato mi ha aiutata a capire e provare lo stress che a volte la ricerca si porta dietro. I suoi consigli sono stati preziosissimi per continuare ogni giorno ed ottenere alla fine importanti e duraturi risultati.

Ringrazio il Prof. Michel DUCLOT e il Dr. Francesco D'ACAPITO che mi hanno dato la possibilità di passare a Grenoble uno dei più fruttiferi e interessanti periodi della mia vita. Sono due grandi *group leader* e *scientist*, ogni giorno mi hanno fatto sentire rilassata e come a casa. I loro preziosi consigli e la loro attitudine all'ascoltare le persone e guidarle attraverso i loro obiettivi sono qualità incredibili e inestimabili.

Ringrazio Marco MOLINARI, Dottorando e compagno di corso, *scientist* infaticabile; le sue notti "brave" avevano un effetto incredibile in quanto era pieno di energia ogni mattina (dopo diversi caffè, ovviamente).

Il Dr. Filippo MAGLIA e il Dr. Marco SCAVINI, due delle persone più divertenti che io abbia mai conosciuto.

Ringrazio il Prof. Giorgio SPINOLO che mi ha insegnato la precisione e l'ordine della ricerca, ogni giorno.

Alice GARBERI e il suo manganato di potassio che mi ha dato l'opportunità di provare la paura e la soddisfazione di essere un *supervisor*; probabilmente la paura era più per lei e la soddisfazione più per me.

Ho apprezzato molto il lavorare vicino al Dr. Michele ZEMA e alla Dr. Serena TARANTINO che hanno collaborato allo stesso progetto.

Devono essere menzionati anche altri membri del gruppo, il Prof. Umberto ANSELMI TAMBURINI e Primo BALDINI, Ilenia TREDICI, post-Doc, e Beatrice MARONI, Dottoranda. Il loro aiuto, le piacevoli chiacchierate e lo scambio di opinioni sono state amichevoli compagne ogni giorno.

Vorrei a questo punto ricordare anche tutta la beamline GILDA e lo staff LEPMI. Ciascuno di loro ha contribuito a rendere il mio soggiorno a Grenoble unico. Vorrei ringraziare inoltre il Dr. Lorenzo MALAVASI.